5-2018

Investigation of Nanomaterial Based Photovoltaic Panel Packaging Materials

Xingeng Yang
University of Arkansas, Fayetteville

Investigation of Nanomaterial Based Photovoltaic Panel Packaging Materials

A dissertation submitted in partial fulfillment
of the requirements for the degree of
Doctor of Philosophy in Engineering

by

Xingeng Yang
Wuhan University
Bachelor of Science in Physics, 2004

May 2018
University of Arkansas

This dissertation is approved for recommendation to the Graduate Council.

Simon S. Ang, PhD
Dissertation Director

Z. Ryan Tian, PhD
Committee Member

Roy C. McCann, PhD
Committee Member

Silke Spiesshoefer, PhD
Committee Member

Abstract

In this research, nanomaterial-based packaging materials for photovoltaic (PV) panels are investigated. A hydrophobic/anti-reflective surface coating which not only repels water from the top glass of a PV panel but at the same time reduces its light reflectance is investigated. COMSOL simulation results indicate that taller ellipsoid rod (aspect ratio = 5) reflects less light than shorter rod (aspect ratio = 0.5) in the desired spectrum for solar energy harvest from 400nm-700nm. The addition of a polymer layer on these ellipsoid rods broadens the light incident angle from 23° to 34°, from which light can be efficiently absorbed. Based on optical simulation results and surface wetting mechanics, the design of a combined anti-reflective and hydrophobic surface for PV panel is investigated. Deep reactive-ion and wet etching are used to fabricate a unique ellipsoid-shaped silicon stamp on a silicon wafer. The nano-imprinting process yields a super hydrophobic silicone coating on glass that can improve light transmittance by 1.5% with a water contact angle larger than 150°. The light transmittance of nano silica coating with a surface assembled monolayer of 1H,1H,2H,2H-Perfluorododecyltrichlorosilane prepared from a sol-gel growth is 3% higher (400nm-700nm) than that for a bare glass slide. This coating passed the MIL-STD-810G felt abrasion test, 100 cycles of temperature cycling test (-45°C-120°C), heat endurance test (200°C for 500 hours), and UV test (2.7mW/cm^2 UVA radiation for 1000 hours).

The second PV packaging material investigated is the nano-particle embedded EVA encapsulation. To block the migration of harmful free radicals that cut the co-polymer network into smaller molecules by chemical reaction in EVA, nano silica particle or

functionalized nano diamond particles are embedded into EVA sheets. A difference of 1% light transmittance between pristine EVA sheet and nano particle embedded EVA sheet indicates that the nano particles slow down the degradation of EVA after 2.7 mW/cm^2 UVA radiation for 2 months. The embedded EVA sheet exhibits better adhesion strength on glass surface indicated by a conventional tape peeling test.

Table of Contents

Table of Figures

Chapter 1. Introduction and Motivations

1.1 Development of Solar Energy

In recent years, environmental stress caused by fossil fuel burning leads to an increasing pursuit of sustainable green energies generated by solar and wind. Electrical energy, in particular from solar energy and in spite of a "production capacity surplus problem" in recent years, undergoes a rapid cumulative 49% annual growth globally since 2003, according to the International Energy Agency Solar PV Technology Roadmap 2014 [1.1]. The percentage of electricity provided by photovoltaic (PV) modules is predicted from about 1% in 2015 to 16% in 2050.

The future of the PV industry appears to be optimistic, however, this does not mean the current PV technologies can support this predicted huge increase. In fact, their low conversion efficiencies and relative high manufacturing costs are preventing the PV panels from being economically sustainable. To find solutions, researches focus on several broad areas. These are:

1) Reduce the cost of materials, so the solar cells can be fabricated economically. For the silicon wafer, these new technologies include, blending in mc-silicon crystallization, the use of diamond saw instead of slurry-based wafer saw to reduce the material lose at the cutting joint, the use of thinner silicon, reduce the silver or aluminum paste consumption for the top contact pattern of the solar cells, etc. [1.2]

2) Design more sophisticated junction structures to improve the light-electricity conversion

ratio. These structures include single-junction, two-junction, three-junction, junction with concentrator, etc. [1.2]

3) Utilize innovative material or packaging structure to increase light harvest and prolong life expectancy of the photovoltaic panels. Anti-reflective coating on the top glass of PV panel is desired to reduce light reflection.

1.2 Research Objective

Among the three aspects of research areas to improving the overall performance of solar or PV panels, this work will focus on the third approach to increase the PV panel packaging efficiency and durability.

In a typical solar cell package, five layers are laminated together to configure a functional and protected solar or PV panel as shown in Figure 1.1. The top layer is a tempered low-iron glass panel and it protects the lower layers consisting of ethylene-vinyl acetate (EVA) encapsulation and solar cells from weathering, and mechanically supports the entire panel. The second and fourth layers are the EVA copolymer encapsulations. They surrounded the entire solar cells to prevent oxygen or moisture from degrading these solar cells and the metal grid on top. It also functions as a shock absorber and an optical coupling layer. The third layer is the solar cell layer, which is in the middle of the five-layered structure. In this layer, solar radiation is converted into electricity by the solar cells. The bottom layer is the back sheet that mechanically supports the entire PV module.

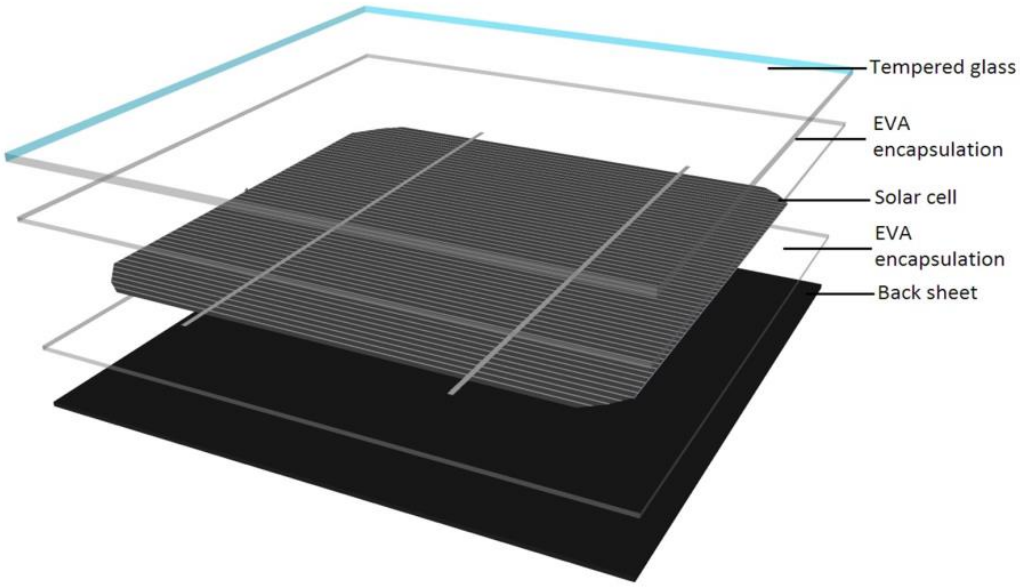

Figure 1.1 A sketch of a typical solar cell packaging

In this five-layer stack, specifically, two individual layers will be studied here. The first is a nano-structured coating on the top glass of the solar or PV panel. This coating will be anti-reflective and self-cleaning. Second, a new nano particles embedded ethylene-vinyl acetate (EVA) encapsulation material will be proposed and investigated.

These two research areas are crucial to the solar industry. First, the coating on the top glass panel manages light in an efficient way. The glass panel is directly exposed to the ambient air. Hence, it is susceptible to environmental contaminates. Many researches indicate that the light blockage caused by the dust accumulation on the tempered glass could degrade its conversion efficiency by as much as 33.5% in one month, and up to 65.8% in 6 months [1.3]. Elminir et. al. [1.4] reported a light transmittance reduction of about 15% in 6 months. Furthermore, light reflection on the interface between air and glass reduces an

additional 4% - 5% of sunlight. This efficiency reduction is too valuable to lose, especially considering the percentage that the industrial PV module efficiency improvement from 2003 to 2012 was just over 5% as shown in Figure 1.2.

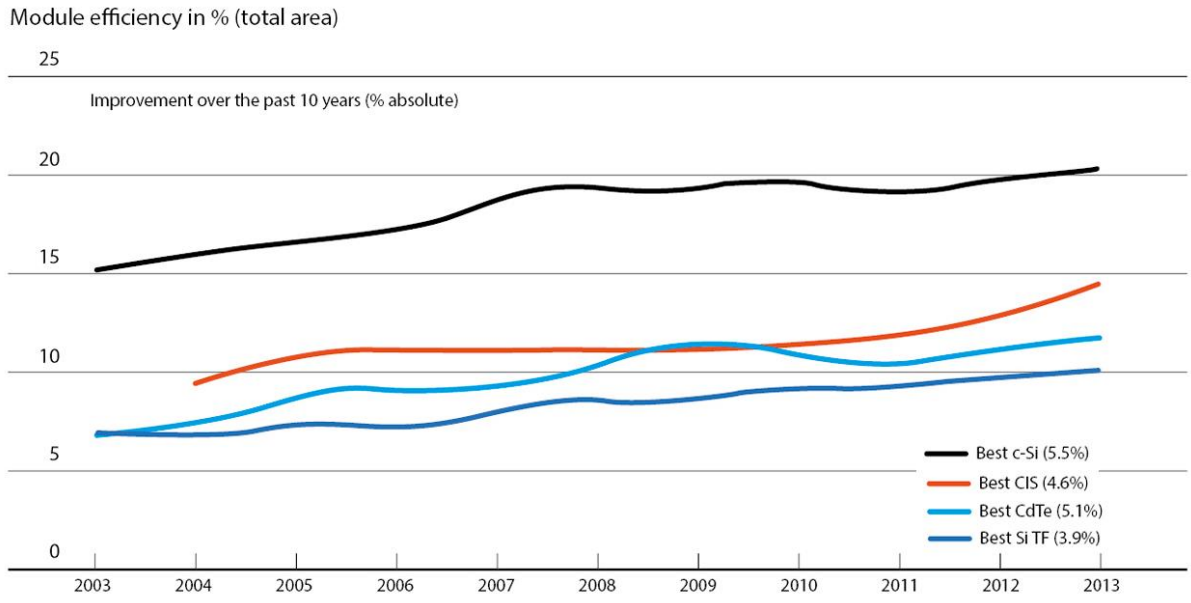

Figure 1.2 Solar photovoltaic module efficiency trends, 2003 to 2012 [1.5]

The solution to the efficiency loss on the tempered glass is an anti-reflective/hydrophobic coating. This coating featured a nano/micro-scaled structure and a low surface energy which not only help to keep the glass surface free of dust but also reduces light reflection as well.

Second, EVA copolymer degrades in climate weathering. In 1990s, more than 45% light transmittance lose was observed in a few years. Later on, various additives were added in to the copolymer. However, the “yellowing” degradation problem remains a major issue that worries solar plants. Here, a new method is proposed to effectively reduce the EVA degradation.

1.3 Brief Overview of Chapters

There are five chapters in this dissertation. Chapter 1 gives the background information on solar cell industry, fundamentals of solar panel, and research objectives. Chapter 2 focuses on the anti-reflective/self-cleaning coating, including the optical theories applied for the anti-reflective coating, the simulation of light transmittance of various nano structure patterned surface based on COMSOL simulation tool, and the physics behind hydrophobic surfaces. In Chapter 3, experimental processes of preparing anti-reflective/self-cleaning coating will be described, tests data will be organized and analyzed, and conclusion will be made. Chapter 4 discusses EVA degradation mechanisms, process of making durable EVA encapsulation, degradation tests, and results and discussion. Chapter 5 concludes the contribution of this dissertation research and gives future research suggestions.

1.4 References

[1.1] “Technology Roadmap Solar Photovoltaic Energy - 2014 edition”, International Energy Agency.

[1.2] “International Technology Roadmap for Photovoltaic (ITRPV), 2015 results including maturity reports”, seventh edition, October 2016.

[1.3] Hassan AH, Rahoma UA, Elminir HK, Fathy AM. “Effect of airborne dust concentration on the performance of PV modules”. J Astron Soc Egypt 2005;13(1):24–38.

[1.4] H.K. Elminir et al. Energy Conversion and Management 47 (2006) 3192–3203

[1.5] Data: Photon 2/2003-2009, Photon Profi 2/2010-2/2012. Graph: Willeke Fraunhofer ISE 2013

Chapter 2. Anti-Reflective and Hydrophobic Surfaces

2.1 Anti-Reflective Surfaces

2.1.1 Light Reflections

Light reflection is a directional change of a light wave front as it propagates to an interface of two different media. Because of this, a certain part of wave front returns back into the media where it originates. Most objects can reflect light. For example, the reflected lights are collected by human eyes so substances that are not light sources can be seen. Another good example of light reflection occurs on mirrors, smooth water or other specular surfaces, on which images of other objects can be formed. These two examples represent two categories of reflection, diffuse reflection and specular reflection.

Both these diffuse and specular reflections can be explained by Laws of reflection derived from Fresnel equations. The Laws of reflection state that the incident ray, normal, and the reflected rays are all in the same plane. The angle between the incident and normal rays is equal to that between the angle between the normal and reflected rays. The incident and reflected rays are on two different sides of the normal ray. In diffuse reflection, the microscopic irregular on the rough surface can be considered as groups of micro-scaled specular surfaces with various tilt angles assembled together. The reflected ray bounces off the surface in different directions, some of them strike the surface material again, and absorbed or reflected. Lambert's cosine law [2.1] gives a common model of diffuse reflection macroscopically.

Light reflection gives our surrounding its appearance and it contributes to human's modern lives, scientific researches, and industries. However, not all the light reflections are beneficial. For example, insects want to hide the reflected light to keep them safe from predators, huge glass wall of sky scrapers cause light pollution problems, and as in this research, light reflection prevent us from harvesting solar energy in an efficient way. Both insects and humans strive to eliminate the unwanted light reflection, but it seems insects are doing better than us.

The following sections discuss different methods of reducing light reflection using artificial technology and from the wisdom of nature.

a) Use Rough Surface to Reduce Light Reflection

As mentioned in the last section, diffuse reflection takes place when light impinges on a rough surface and a proportion of the reflected light is absorbed by the adjacent bumps. This increases light absorbency on the rough surface. This technology is widely used on solar cells to reduce the reflection on the silicon surface from more than 30% to less than 10% [2.2]. Alkaline solutions such as potassium hydroxide (KOH) can be used to etch the silicon surface into micron sized pyramid shaped structures. In this method, surface roughness contributes to reduce light reflection.

b) Single-Layer Anti-Reflective Coating

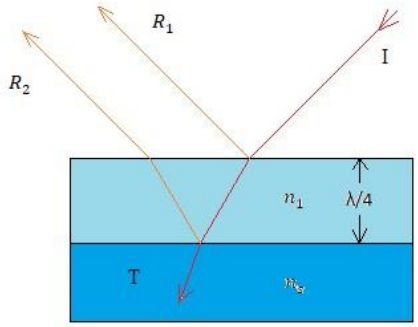

Figure 2.1 Sketch of single layer interference anti-reflection coating

This single layer interference anti-reflective coating employs a thin layer of material with reflective index of n_1 on the substrate with a reflective index of n_s as shown in **Error! Reference source not found.**. [2.3] Two reflected lights will interfere with each other due to the same frequency. If the thickness of the n_1 layer is selected such that the phase difference between reflected ray R_1 and R_2 is half a wavelength, then the superposition of the two rays will be destructive. This means that less or no energy will be reflected. The optimal thickness of the coating should be one fourth of the wavelength of the ray. Normally, in a broad wavelength application, a middle wavelength is used to obtain an overall better anti-reflection effect over a broad spectrum. This technology requires accurate control on the thickness of the coating.

c) Index Matching

Like the interference layer discussed in (b), the index matching technique utilizes a thin film on the substrate. When light incident in the normal angle, the reflectance at the interface is given by Fresnel equation:

$$R = \left(\frac{n_0 - n_s}{n_0 + n_s}\right)^2 \tag{2.1}$$

This equation indicates that if the difference of refractive index (RI) of adjoining media is small, the reflectance is small. The same rule applies on the general incident situation, that is, for a ray with any incident angle, a smaller RI difference will yield a weaker reflectance. It can be shown that the total reflection in the presence of the thin layer with $n_1$as shown in Fig. 2.2 [2.3] is given as

$$R_{01}I + R_{1S} \cdot T_{01} \cdot I < R \cdot I \tag{2.2}$$

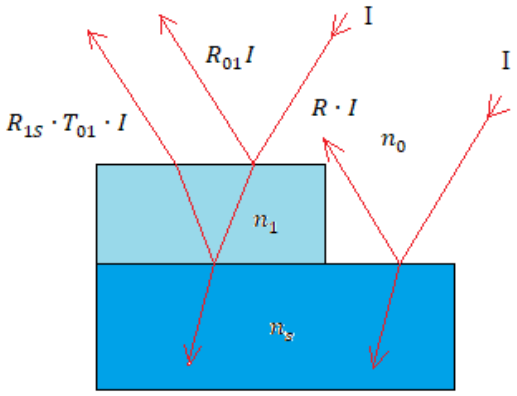

Figure 2.2 Sketch of single layer anti-reflection coating

To obtain the best optical coupling effect, it is important to choose the right material. The optimal value of the RI of the thin film is,

$$n_1 = \sqrt{n_0 \cdot n_s} \tag{2.3}$$

The RI of glass is around 1.5, and air is 1. So, the RI of the thin film anti-reflective coating on glass should be about 1.23, which is much lower than all the materials we know. In industry, materials with lowest RI are used as anti-reflective coating on glass, such as magnesium fluoride [2.4].

d) Moth's Eye Structure

To enhance performance, anti-reflective coating usually combines interference and index matching in one layer. The coating thickness is one fourth of the middle wavelength of incident light and with a RI equals to the square root of that of the substrate. If roughness is introduced into the coating, then the low refractive index coating can be hundreds of nano meters thick. That is exactly what nature gives insects the moth's eye structure as shown in Fig. 2.3 for instance. This structure contains all the three elements discussed in the artificial anti-reflection coatings.

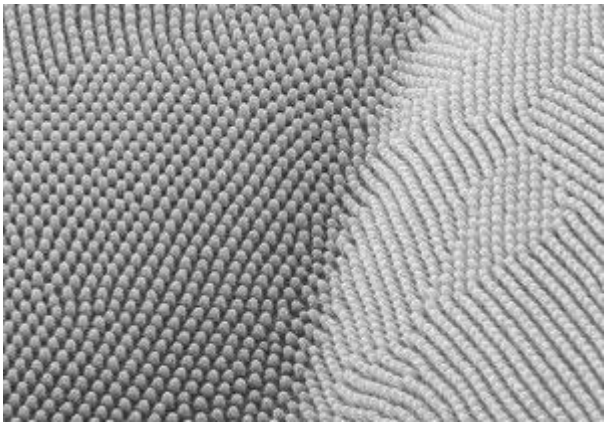

Figure 2.3 Moth's eye structure [2.5]

These arrays of nano sized tapered protuberance on the moth's eyes are about 200nm tall and with the same length of period. Using this structure as a camouflage, moths reduce the light reflection on their eyes to prevent them being found by their predators, such as owls. Unlike the single layer anti-reflective (SLAR) coatings, which perform within a narrow spectrum, the moth's eye structure efficiently reduces light reflection over a broad bandwidth and angle. The structure of moth's eye has been discovered and studied for decades. In 1967, Bernhard first found the corrugation and proposed that the tapered bumps

form a graduate change of refractive index, which explains the broad bandwidth anti-reflective property [2.5]. The basic principle and physics behind the phenomenon has been understood for a long time. One of the best theories is the effective medium theory or effective medium approximations. [2.6]

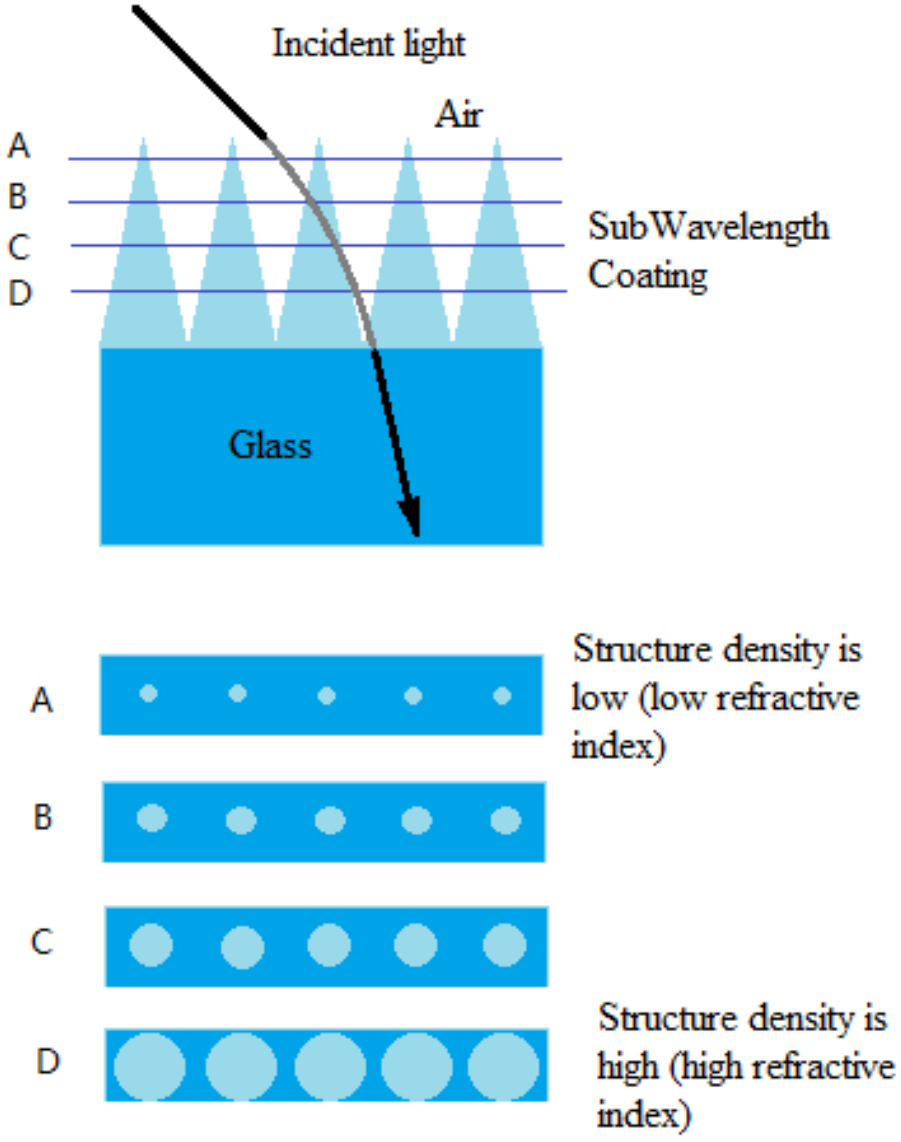

Figure 2.4 Illustration of effective refractive index [2.6]

The effective medium theory uses an effective refractive index to describe macroscopic optical properties of inhomogeneous media. In a composite material, for example glass and

air (holes) composed of tapered nano protuberance as shown in Figure 2.4, its effective refractive index can be approximated to describe the overall RI of the composite. Specifically, in this figuration of the bumps, every horizontal layer of the material can be considered as a homogeneous plate. Suppose there are four planes labeled A, B, C, and D that cut through the tapered structure, then there are four cross sections indicated in the low portion of Figure 2.4. Each cross section consists of different portions of glass and air. If we know the exact percentage of the glass material or the air, then the overall RI of the cross section can be calculated. In cross section A, the glass takes only a little portion of the area due to the shape of the protuberance, as such, the effective RI is predominantly dominated by the RI of the air. While for the plane D, the glass density is very high compared with the air, then the effective RI is close to the glass. If the cutting planes are myriad instead of the four A, B, C, and D planes, the effective RI would continuously increase from 1 (RI of the air) to 1.5 (RI of the glass). This graded refractive index reduces light reflection in two ways. First, because the differences between RIs of each adjacent cross section are very small, according to equation 2.1, the reflection between these two cross sections is very low, so is the overall reflection. Second, light propagates from optically thinner media to thicker media on each interface of different cross sections, so the incident angles are larger than the refracted angles. This results in bending of the light toward the normal direction. The change of incident direction further reduces the reflection.

Many industrial applications make used of this optical property of sub-wavelength structure. For example, the AR coatings on eyeglasses, optical lenses, solar panels, etc. Intensive

researches are carried out to develop technologies of this artificial optical media. These technologies generally include microelectromechanical systems (MEMS) methods, nanoimprint process, and sol-gel approach. As for solar power industry, a high yield and low cost coating is desired, as such nanoimprinting and sol-gel process are being studied.

2.1.2 Anti-Reflective Surface Structure Design Based on COMSOL Simulation

a) COMSOL Simulations

COMSOL Multiphysics Modeling Software (wave optics module) [2.7] can be used to simulate light reflection on different surfaces with various configurations of nano structure or with a silicone layer covering the nano structures to mimic the two-layer structure of an anti-reflective/hydrophobic surface.

In COMSOL simulations, the structure dimensions, materials properties, boundary conditions, and formulas are first defined. Then meshing is defined, followed by the simulation and plotting. In the appendix, simulation of light reflectance of a surface with ellipsoid roughness (Figure 2.5) is explained with details. The sketch shows a nano structured hemisphere coated on a glass square column. In a practical application, there are actually billions of the hemispheres built on the glass substrate. For the calculation convenience, only one smallest periodic unit of the whole structure is considered. To understand how the aspect ratio of the nano structures affects the light reflectance, three configurations of the structure are studied with the simulation software. The aspect ratio of them are 0.5 (Figure 2.5), 2.5 (Figure 2.6), and 5 (Figure 2.7) respectively. Besides the simulation of these three configurations (results are plotted in Figure 2.8 as a, c, and e),

three more structures are investigated. There three structure are with an additional polymer coating on the ellipsoids compared with a, c, and e. The simulation results are numbered as b, d, f in Figure 2.8.

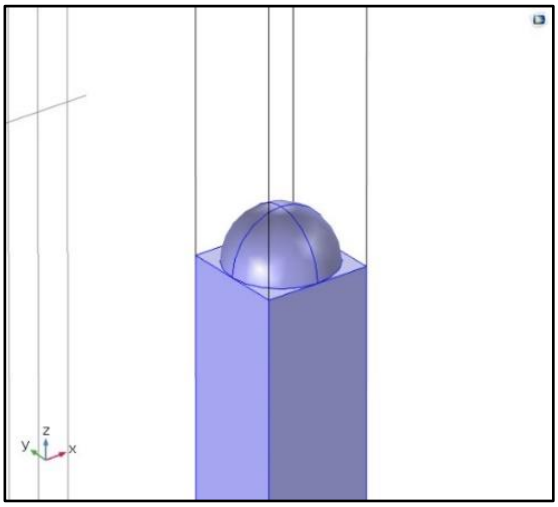

Figure 2.5 Sketch of a nano structure (aspect ratio: 0.5) coated on glass substrate

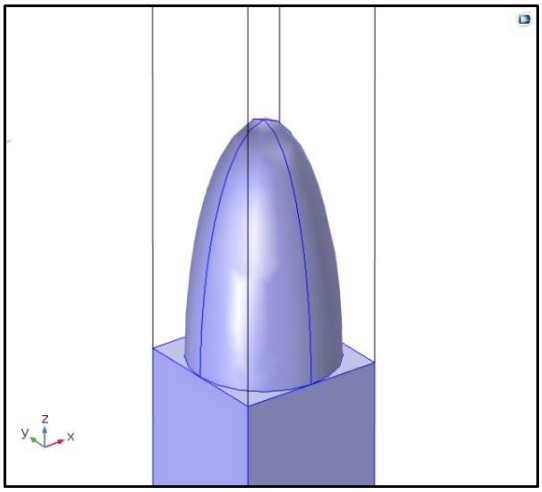

Figure 2.6 Sketch of a nano structure (aspect ratio: 2.5) coated on glass substrate

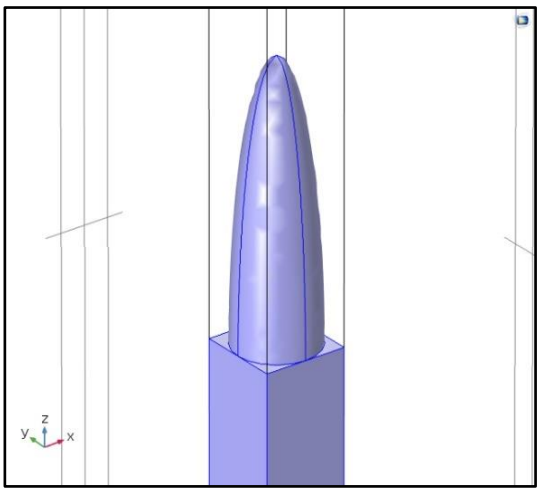

Figure 2.7 Sketch of a nano structure (aspect ratio: 5) coated on glass substrate

b) Simulation Results

The simulation results are plotted in Figure 2.8 (a) and (b) to show the reflectance base on the same dimension of the roughness, periodic semi-ellipsoid structures with a diameter of the base section of 0.33 micron and a height of 0.17 micron.

The different between Figure 2.8(a) and (b) is that there is an additional silicone layer on structure Figure 2.8 (b). The same differences are for Figure 2.8 (c) and (d), as well as Figure 2.8 (e) and (f). The semi-ellipsoids shown in Figure 2.8 (c) and (d) are 0.85 microns in height and 0.33 micron in width. This is the same foot print as sample shown in Figure 2.8 (a) and (b), but five times taller in height. Samples shown in Figure 2.8 (e) and (f) are 10 times taller but having the same width as those shown in Figure 2.8 (a) and (b).

c) Discussion

There are distinct differences in reflection between the samples with silicone coating (b, d, f) and those without silicone coating (a, c, e).

As shown, there is a strong reflection occurring at about 400 nm at 0.6 rad (about 34°) incident angle. This wavelength is crucial in the absorbing range of solar cell absorption spectrum. As such, a relative high reflectance lowers the efficiency of the solar module. Based on these results, it can be concluded that a thin layer of silicone layer can increase the performance of the solar panel at a larger incident angle.

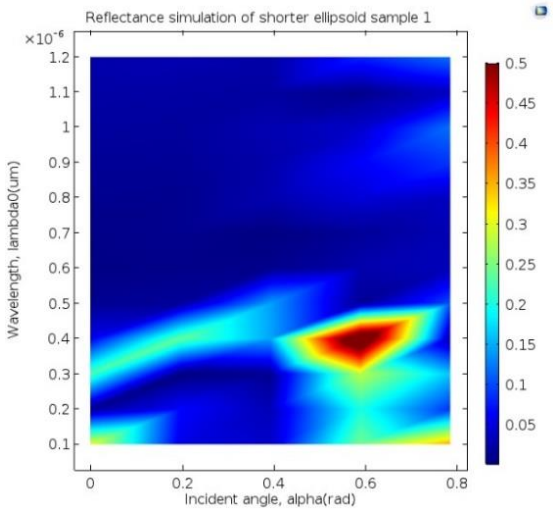

(a)

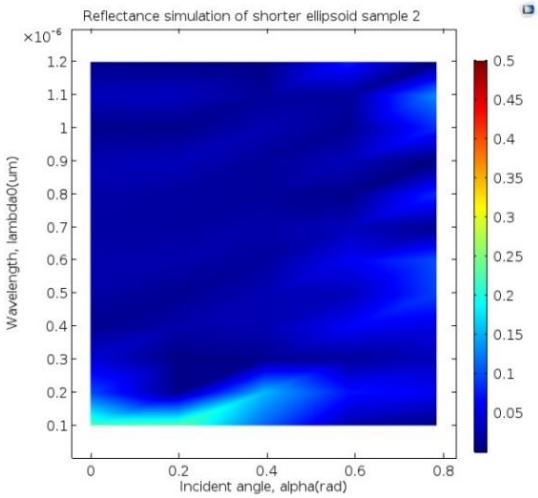

(b)

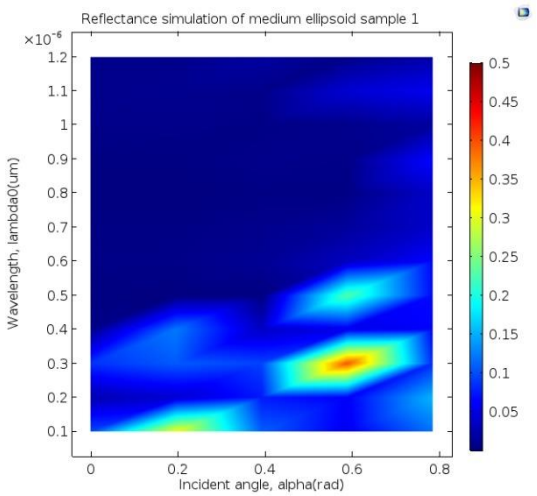

(c)

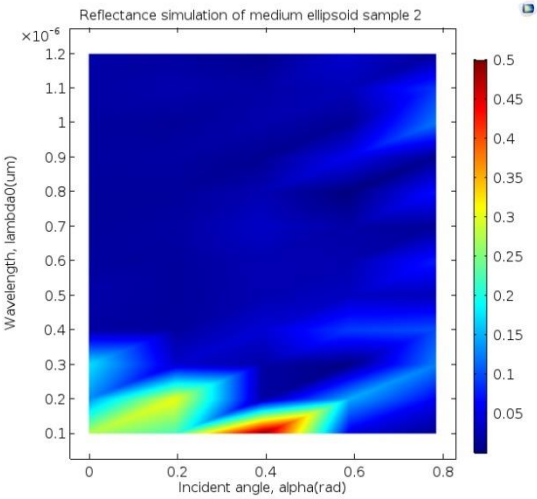

(d)

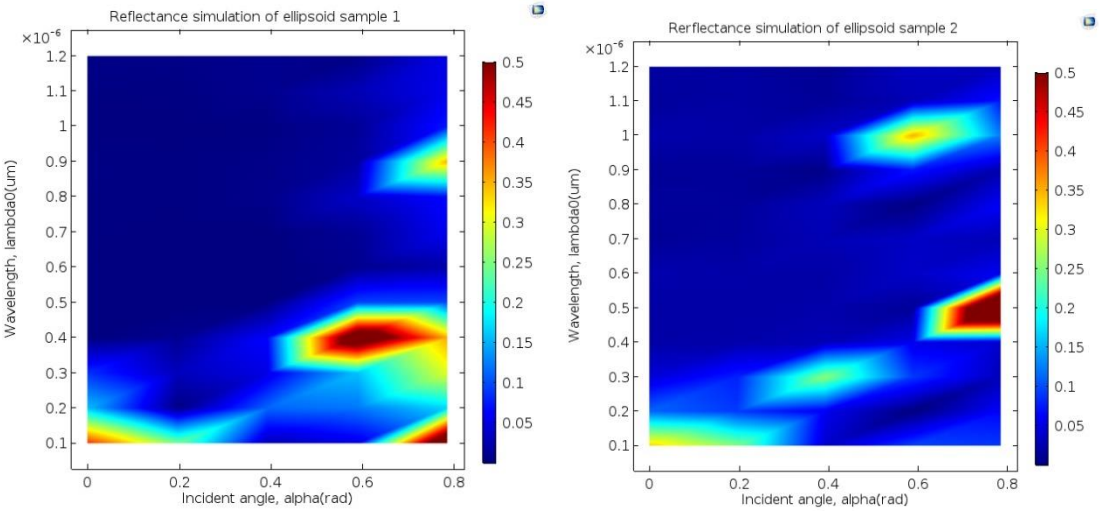

(e) (f)

Figure 2.8 Simulation results of light reflectance on different surfaces

As shown in Figure 2.8, at wavelength longer than 300nm with incident angle less than 0.4 rad or about 23°, the light reflectance reduces as the semi-ellipsoids become taller. This means that tall semi-ellipsoid structures increase the light absorbance and favors the solar panel overall efficiency. The surface structure with the best absorbance would be the slender needle structure. However, considering the difficulties of a practical manufacturing process and the fragile nature of the slender structure in practice, the semi-ellipsoid structure cannot be built too tall.

As shown in Figure 2.8, samples (b) and (d) show a strong reflectance below 300 nm at an incident angle below 0.6 rad (about 34°). This indicates that more light below 300 nm is blocked by the EVA encapsulation in the solar panel from degradation. Ultra-violet (UV) radiation plays a crucial role in degradation to the EVA and solar cells.

2.2 Hydrophobic Surfaces

2.2.1 Introduction: Surface Wetting and Its Measurement

a) Wetting on Ideal Solid Surface

Surface wetting measures the ability of a liquid to maintain its contact with a solid surface. When a liquid drop sits on top of a solid surface, it undergoes two forces. One is the adhesion forces between liquid molecules and solid molecules. This force pulls the liquid outward and spread the liquid across the solid surface. The other is the cohesive force. This is the force inside the liquid and it strives to shape the liquid into a sphere. For a combination of liquid and solid, one of these forces prevails to a certain degree and as such, the liquid is shaped accordingly to be a perfect ball, a flat plate, or anything in between. If liquid has very little contact with the solid surface in the form of a perfect ball, this is perfect wetting or complete wetting. On the contrary, if the liquid spreads out completely, it is perfect non-wetting. Any wetting between these two can be called partial wetting. Contact angle (CA) is used to quantitatively describe the wetting property of a liquid on a solid surface.

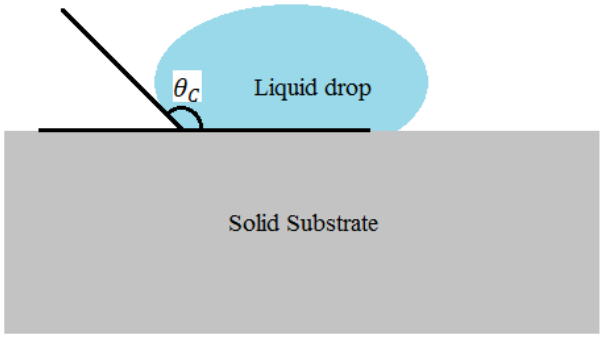

Figure 2.9 Illustration of contact angle

Contact angle forms by the liquid-air interface and the liquid-solid interface is shown as θ_C in Figure 2.9. If water contact angle is less than 90°, the surface is called hydrophilic to the liquid; If CA is between 90° and 150°, it is called hydrophobic. If it is larger than 150°, it is known as super hydrophobic. The properties of liquid, internal properties of the solid surface, and structure of the solid surface determine the contact angle. In the photovoltaic panels, the main purpose of the top coating is to repel water, so our investigation focuses on the material properties and the surface structure that yields a hydrophobic or super hydrophobic surface.

To study solid surface properties, concept of ideal solid surface is introduced. The surface is assumed to be perfectly flat, hence the effect on WCA made by the surface roughness is neglected. The chemical properties of the surface are homogeneous, and with no WCA hysteresis, which means the advancing and receding angles are equal. As such, surface energy is the predominant factor to affect the surface wetting property. Solids can be categorized into high surface energy or low surface energy. For example, glass, metal, and ceramics are very hard with strong chemical bonds (ionic, metallic, or covalent). As such, large energy is needed to break these bonds, so they are called high surface energy solids. Other solids are hold up by weak bonds such as hydrogen bonds and van der Waals force. Weak forces can separate these solids, for example some polymers, they are called low surface energy solids.

On an ideal solid surface, magnitudes of surface energy determine water contact angles (WCAs). When the bond forces in these solids are much larger than the hydrogen bond in

water, the molecules of the surfaces "pull" water molecules to spread out as a thin plate on the surfaces, these forces prevail the bond force of water which fights against the surface forces and trying to "ball up" the water drops. These surfaces are hydrophilic to water. For some chemical bonds that not as strong as the hydrogen bonds in water, they hardly affect the shapes of the water drops, the water drops will hold together as a sphere on the surfaces. These solid surfaces are hydrophobic. [2.8]

b) Wetting on Non-Ideal Rough Solid Surface

In practice, no surface is perfectly smooth and as such the wettings are complicated by its surface roughness. For example, in the lotus leaf structure, a typical hydrophobic surface in the nature, water is repelled from wetting itself though its rough and wax-coated surface. This lotus surface is intensively studied and many models are proposed to explain their wetting properties. Among these models, two of them are widely accepted. The first model is given by the Wenzel's model [2.8] and is given by:

$$\cos\theta^* = r\cos\theta \qquad (2.4)$$

The second model is given by the Cassie-Baxter model [2.8]:

$$\cos\theta^* = r_f f\cos\theta^Y + f - 1 \qquad (2.5)$$

In the Wenzel's model, θ^* is the WCA of a textured rough surface,θ^Y is the WCA of an ideal solid surface made with the same material but without any textures or heterogeneity on the surface. r is the roughness ratio and it is defined as the ratio of the true surface area to its projection, as such it is always greater than 1. The equation suggests that if θ is less than 90°,

then θ^* is less than θ; if θ is larger than 90°, then θ* is larger than θ. From the above, it is clear that introducing roughness onto a perfect hydrophilic surface will make the surface more hydrophilic, while introducing roughness onto a perfect hydrophobic surface will make the surface more hydrophobic. As such, the factor *r* measures how roughness effects on a perfect solid surface.

Compared to the Wenzel's model, Cassie-Baxter model provides a better modeling when deal with a heterogeneous surface. In equation (2.5), similar to the *r* in the Wenzel's model, r_f describes the roughness ratio, *f* is the proportion of solid surface area that wet by the liquid.

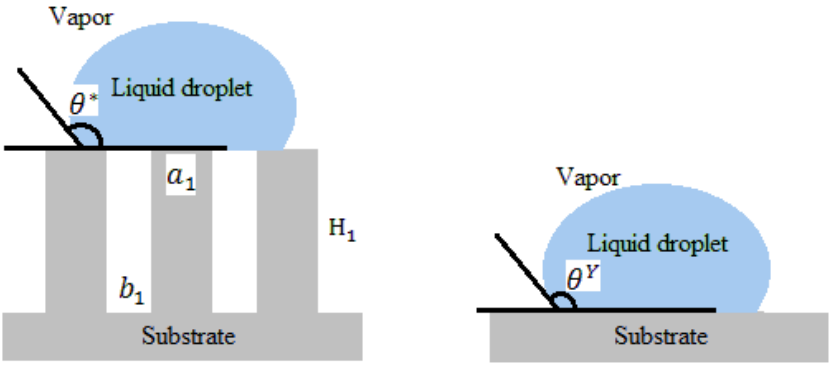

Figure 2.10 Cassie-Baxter model [2.8]

Figure 2.10 shows a sketch of wetting on a surface with rectangular roughness. The width, spacing, and height of the bumps are a_1, b_1, and H_1. Then, f is,

$$f = \frac{1}{[(b_1/a_1) + 1]^2} \tag{2.6}$$

Equation (2.6) indicates how the configuration of the protuberance affects the parameter f, and WCA. If a_1 goes small, then f becomes small, then the value of $cos\theta^*$ decreases and this will result in a larger WCA θ^*.

Both the Cassie-Baxter and Wenzel models enlighten many designs of hydrophobic surfaces. In applications, the WCA larger than 150° (super hydrophobic) is preferred, surface with such high WCA shows non-wetting and self-cleaning capabilities. To achieve the WCA above 150°, low surface energy material is needed. Polymer material has the lowest energy, the WCA of perfect polymer surface range from 100° to 110°. Based on these WCAs, according to calculation, an aspect ratio of surface nano-scaled configuration need to be larger than 5 to increase the actual WCA to 150°. This is very challenging to create such slender rods from soft polymers. A new angle to approach super hydrophobicity without building tall and fragile rods is needed. Luckily, the microscopic structure of lotus leaves gives clues to this approach.

2.2.2 The Lotus Leaf Structure

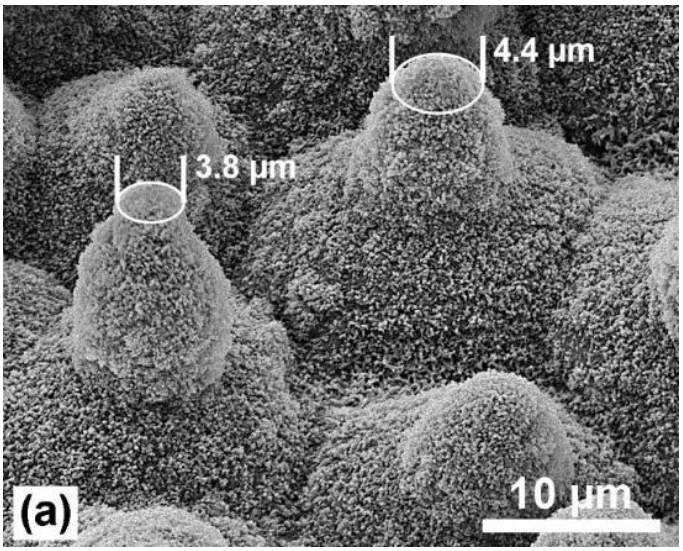

Figure 2.11 SEM imagine of lotus leaf surface structure [2.9]

Hydrophobicity has been studied half a century ago. In 1977, Barthlott and Ehler [2.10] studied the self-cleaning effect of lotus leaf structure and they called this water repelling phenomenon as the lotus effect. Later in 1980s, chemists and biologist begin to apply the lotus effect to handle fluid. In recent two decades, the application of lotus effect on self-cleaning, protective coatings has emerged.

The microscopic structure of lotus leaves is well studied. There are arrays of papillae on the lotus leaves, with 10 to 20 micron in height and 10 to 15 micron in width as shown in Figure 2.11 [2.9]. Beside this micron scaled roughness, epicuticular wax coated nano rods are grown on the micro papillae. This lotus structure inspires a new approach to create super hydrophobic surfaces without elaborate processes.

The lotus structure has a two-scaled roughness consisting of both micron and nano sized configurations on the surface. Because water droplets (size of rain drops are around 0.5 mm

to 4 mm, the tiny droplet in cloud, fog, mist are around 10 to 15 microns in diameter) are a few orders of magnitude larger than the nano rods on the lotus leaves, these water droplets cannot "see" these nano rods. As such, this nano rod coated surface is an ideal solid surface with a higher WCA than any known polymer. If this ideal surface is shaped with micron scaled protuberance, the overall WCA will be greater than 150°. In another word, if the factor *f* (configuration of the micro scale roughness) is not changed, an ideal polymer coated nano rods can be formed. This results in a larger θ^Y, which ultimately obtains a larger θ^*.

$$\cos\theta^* = r_f f \cos\theta^Y + f - 1 \qquad (2.7)$$

2.3 Design of New Rough Hydrophobic/Anti-Reflective Surface

To design a surface with both hydrophobic and anti-reflective properties, we need to combine the two desired structures that discussed in section 2.1 and section 2.2 into one structure. According to the analysis in the section 2.2, for a hydrophobic surface, a desired microscopic structure, as showed in Figure 2.12 (a), should meet the following requirements. (i), the pillars are with high aspect ratio, (ii) there are nano-scale roughness on the surface of pillars, (iii) surface energy is low, (iv) the pillars are properly spaced apart, (v) the size of the structures are below 10 microns.

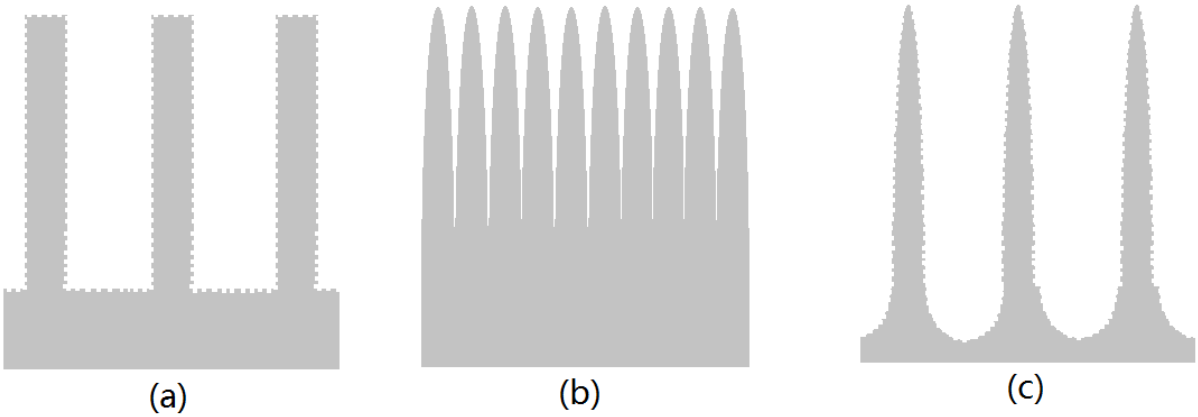

Figure 2.12 Design of a hydrophobic/anti-reflective surface

As for an anti-reflective surface structure, the requirements are different (showed in Figure 2.12 b). (i) The prominences are shaped as ellipsoid, but not pillar, (ii) there is no space between the ellipsoid prominence, so the light reflection from the flat surface between the prominence can be eliminated, (iii) the surface roughness or low energy is not necessary, (iv) the dimension of the roughness is hundreds of nanometers.

If we put the requirements of Figure 2.12 (a) and (b) together, a structure showed in Figure 2.12 (c) meets all the criteria of (a) and (b) at the same time. The structure in the Figure 2.12 (c) should be with these properties. (i) high respect ratio ellipsoid prominence, (ii) there are spaced out with a proper distance, (iii) the whole surface is with nano-scaled surface roughness and low surface energy, (iv) the flat valley floor between ellipsoids should be shaped as inverted ellipsoids, (v) the dimension of the roughness is hundreds of nanometers.

In the next chapter, experimental methods of fabrication this designed nano structure will be discussed, and the prepared samples will be tested and studied.

2.4 References

[2.1] Wikipedia, “Lambert’s cosine law”.

[2.2] D.H. Macdonald, A. Cuevas, M.J. Kerr, C. Samundsetta, D. Ruby, S. Winderbaum, A. Leo, “Texturing industrial multicrystalline silicon solar cells”, Volume 76, Issues 1–3, January–March 2004, Pages 277–283

[2.3] Wikipedia, “Anti-reflective coating”. 2017

[2.4] Michael Fink, “Types of anti-reflective treatments and when to use them”, the photonics solutions update, p 28-31

[2.5] Michael Berger, “Moth eyes inspire self-cleaning antireflection nanotechnology coatings”, nanowerk, Oct, 28, 2008

[2.6] Hemant Kumar Raut, V. Anand Ganesh, A. Sreekumaran Nair and Seeram Ramakrishna, “Anti-reflective coatings: A critical, in-depth review”, Energy Environ. Sci., 2011, 4, 3779.

[2.7] Comsol, “Wave optics module,for simulating electromagnetic wave propagation in optically large structures”, https://www.comsol.com/wave-optics-module, 2017.

[2.8] Wikipedia, “Wetting”, 2017

[2.9] Sanjay Lakshmanan, “An analysis of hydrophobic fabric using electron microscopy”, http://www.optics.rochester.edu/workgroups/cml/opt307/spr16/sanjay/IndexNew.html.

[2.10] Barthlott, Wilhelm; Ehler, N. 1977. "Raster-Elektronenmikroskopie der Epidermis-Oberflächen von Spermatophyten". Tropische und subtropische Pflanzenwelt. Akad. Wiss. Lit. Mainz. 19: 110, 1977

Chapter 3. Fabrication and Characterization of Anti-Reflective & Hydrophobic Surfaces

3.1 Nano Silica Based Anti-Reflective and Hydrophobic Surfaces

3.1.1 Preparation of Nano Silica Based Anti-reflective and Hydrophobic Surfaces

There are two major steps to create a nano silica based anti-reflective and hydrophobic surface. First, a scaled roughness of nano silica layer is coated onto the glass. Second, a self-assembled monolayer is grown on top of this nanosilica layer.

a) Experiment Preparation

Experimental Cleanliness is crucial to the process. All experimental glassware must be cleaned with VWR Labtone solution consisting one oz. of the compound in two gallons of water. Properly cleaned glassware retains a thin water layer on its surface and this water does not flow down as a stream but rather hangs onto the glass surface as a water drop. Glassware that does not shows this property after the soap cleaning cannot be used in the process. The contamination on experimental glassware changes the wetting properties which makes the nano silica film non-uniform in the spin coating process. Moreover, it further poisons the SAM growing solution and makes the layer non-uniform.

Silica nano particles with particle size between 5nm and 10nm in diameter, gama-glycidoxypropyltrimethoxysilane, formic acid, tridecafluoro-1, 1, 2, 2, -tetrahydro-octyltrichlorosilane [CF_3 $(CF_2)_5(CH_2)_2SiCl_3$, FOTS], hexadecane, and carbon tetrachloride are purchased from Sigma Aldrich. Polystyrene nanoparticle aqueous suspension (7 microns in diameter, 5% weight) is acquired from Spherotech Inc.

b) Nano Silica Coating Process

For the first nano silica layer, polystyrene nano particles were used as templates to create a surface with different configurations onto the nano silica particle coating. A sol-gel process was employed [3.1]. Nano silica particles are first dissolved in an ethanol/water mixture (10g:1g) and dispersed using ultra-sonication for 10 minutes. Then 0.05g formic acid and 0.05g of (3-Glycidyloxypropyl)trimethoxysilane are added. After ultra-sonication for another 10 minutes, the mixture is stirred at 40°C overnight. Then, 2 mL of 5% weight of polystyrene beads suspension is added and ultra-sonicated for 10 minutes, which is followed by a spin coating process for 30 seconds at a spin rate of 6000 rpm. Lastly, the coated glass slides are dried in air atmosphere and calcinated at 500°C in an oven for 60 minutes to burn out the polystyrene particles.

Weighing the nano silica particles needs extra attention due to its environmental concerns. As such, it is performed in a fume hood. Before weighing, the fume hood is cleaned thoroughly. After this, water saturated paper sheets are placed on the fume hood to fully cover the entire working surface inside the fume hood. After that, the venting fan of the fume hood is switched off and nano silica powder is weighed using a chemical balance. The nano silica particles with be blown and contaminate the entire fume hood chamber. After weighing, the nano silica powder is covered and the fume hood is cleaned with wet paper.

In the silica calcination process, a furnace is first calibrated with a thermal couple and the calcination process is carried out using the furnace temperature profile as shown in Figure 3.1.

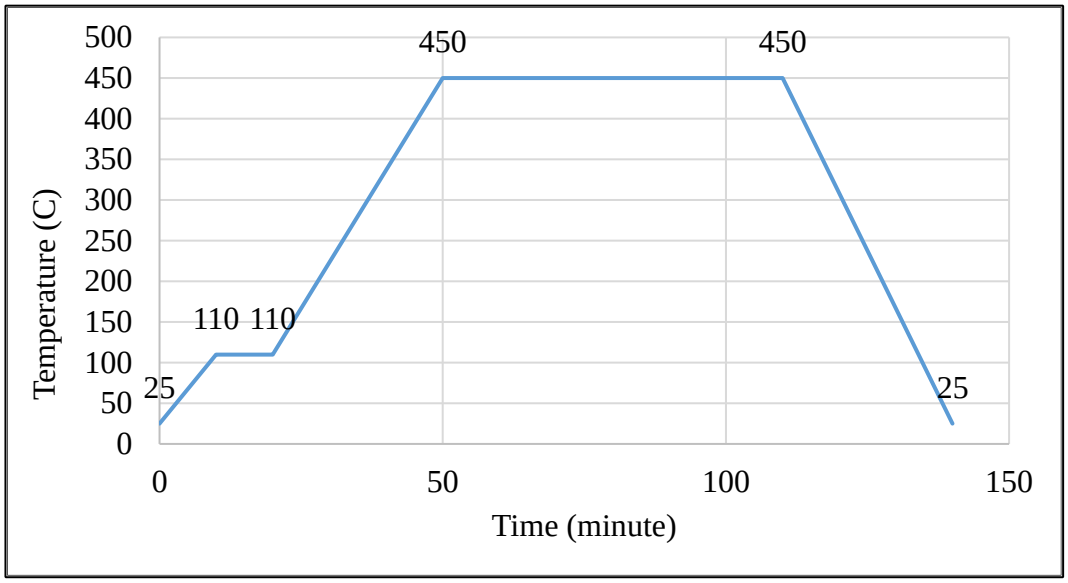

Figure 3.1 Thermal profile of silica calcination process

For a uniform coating, the spin process recipe consists of several stages as shown in Table 3.1.

Table 3.1 Spin coating recipe

Stage	Revolutions per minute (rpm)	Ramp time (seconds)	Duration	Process
1	100	1	3	Apply Solution
2	0	0.1	2	Coverage
3	150	0.1	2	Coverage
4	0	0.1	2	Coverage
5	800	1	5	Spread out
6	6000	1	45	Settlement
7	1500	2	10	Recovery
8	0	2	3	End

At stage one, while the glass substrate rotates at a slow rate on the chuck of the spin coater, coating solution is dispensed onto the central part of substrate using a burette. After that, the

substrate rotates and stops twice from stage 2 to stage 4. This motion shakes the coating solution and distributes it uniformly onto the entire glass substrate. Then the spin rate increases to 800rpm at stage 5 to shake off the excess coating solution from the glass substrate, and leaves only a thin uniform layer on the glass substrate. At stage 6, the spin rate is set to the highest spin speed that determines the thickness of the film. Last, the glass substrate spins at 1500rpm to compensate the non-uniform thickness on different glass substrate areas. The centrifugal force on each point on the glass substrate is proportional to the distance between this point and the rotation center. This results in a larger centrifugal force in the center than that in its periphery. Reducing the spin speed increases the uniform distribution of centrifugal force, hence, making the thickness more uniform on the entire glass substrate.

In general, thickness of spin coated film is inversely-proportional to the square root of angular velocity [3.2] given by

$$t \propto \frac{1}{\sqrt{\omega}} \qquad (3.1)$$

In the experiment, different spin rates are applied at the stage 6 to obtain coatings with different thickness. The spin rates are 1000, 2000, 3000, 4000, 5000, 6000, and 7000 rpm. Before the spin coating process, small pieces of Kapton tapes are attached onto the glass substrate. After coating, the tapes are removed. This tape forms a step with and without nano silica film. These steps are used for the measurement of thickness using a surface profilometer.

c) SAM Growing Process

The coated glass substrates are rinsed in DI water, methanol, and carbon tetrachloride sequentially for 15 minutes at each step. After, the substrates are immerged in 50 mL of tridecafluoro-1, 1, 2, 2, - tetrahydro-octyltrichlorosilane precursor solution (0.05mL FOTS, 40mL hexadecane, and 10mL carbon tetrachloride). Then, samples are took out of the solution and cleaned in carbon tetrachloride, methanol, and DI water sequentially. Lastly, the SAM layers are cured at 150°C for 10 minutes. The glass beakers used in the process are kept still to prevent any disturbance of the solution, this helps to maintain the uniformity of the SAM layer. All these steps are performed inside a fume hood and a full-face mask along with a cartridge respirator. Glass substrates are handled with a stainless-steel tweezers which is also cleaned with acetone, IPA, and DI water.

Growing time is an important parameter for the density of the SAM layer on the nano silica coated surface. Samples are kept in solution for from zero minute to 20 minutes.

3.1.2 Measurements of Coated Nano Silica Surfaces

The thickness of nano silica coating is measured using a Dektak 3030 profilometer with a measurement range of 50Å to 1,310Å. A VCA Optima video contact angle system is utilized to measure the water contact angle on the prepared samples. A DU 730 Life Science UV/Vis Spectrophotometer (Beckman Coulter) is used to measure the light transmittance of samples.

3.1.3 Measurement Results and Discussion

a) Concentration of Nano Silica Solution versus Film Thickness

According to the simulation results discussed in Chapter 2, the thickness of nano silica coating should be less than 200nm. Spin speed and concentration of the nano silica solution are controlled to yield different thicknesses of coated nano silica film.

The maximum spin speed for the 6800 Spin Coater Series (Special Coating Systems) is 7000rpm. At this spin speed, the vacuum holds the glass substrates firmly during spinning. The thickness of the coated film is 200nm when a nano silica solution with a 10% (by weight) concentration is coated onto the glass substrates at 7000rpm. For a thinner silica coating, less concentrate nano silica solutions are prepared while the spin coating speed is kept at 7000rpm. Six samples are prepared according to the recipes shown in Table 3.2

Table 3.2 Coating recipes of the samples

	Sample 1	Sample 2	Sample 3	Sample 4	Sample 5	Sample 6
Concentration of nano silica solution (weight %)	10.0%	6.15%	4.44%	2.76%	2.00%	1.60%
Spin Speed(rpm)	7000	7000	7000	7000	7000	7000

Thicknesses of the coatings on samples 1, 2, 3, 4, 5, and 6 are measured and are shown in Figure 3.2 to Figure 3.7.

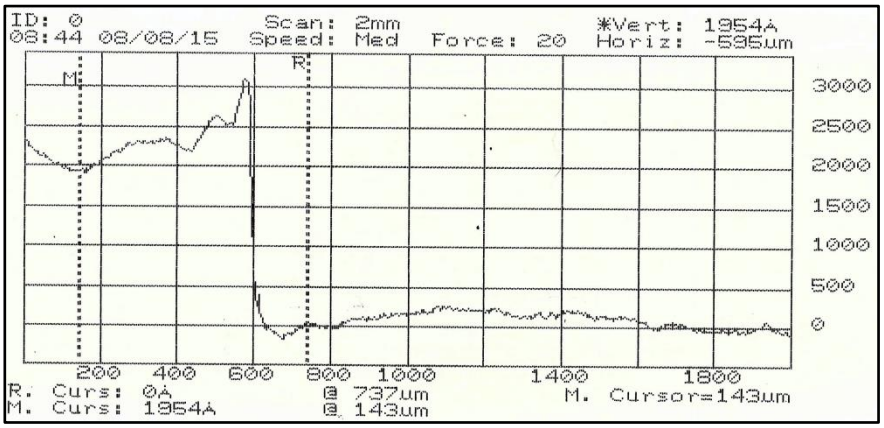

Figure 3.2 Thickness measurement of sample 1 is 195nm

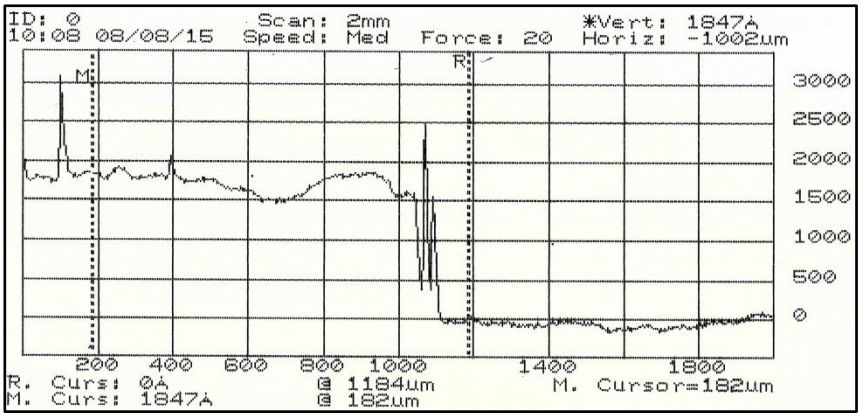

Figure 3.3 Thickness measurement of sample 2 is 185nm

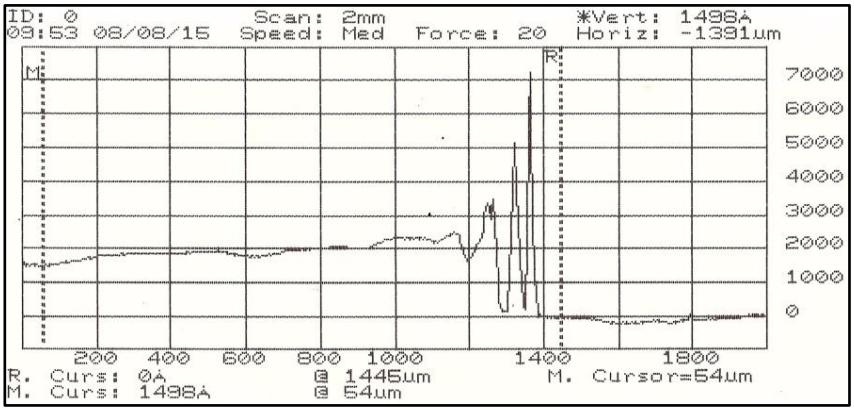

Figure 3.4 Thickness measurement of sample 3 is 150nm

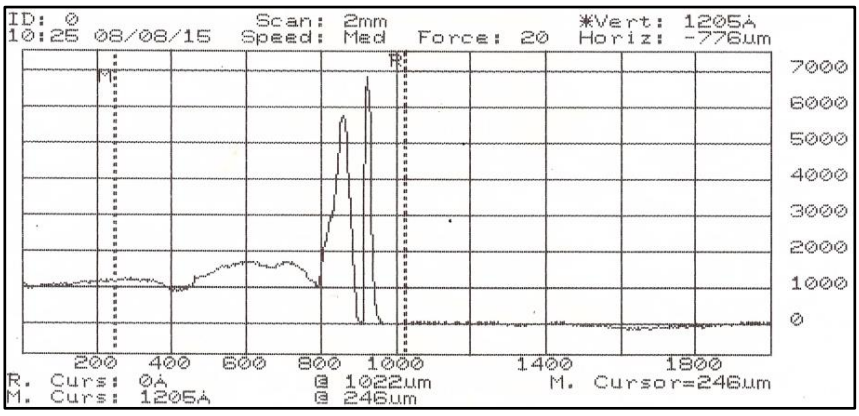

Figure 3.5 Thickness measurement of sample 4 is 120nm

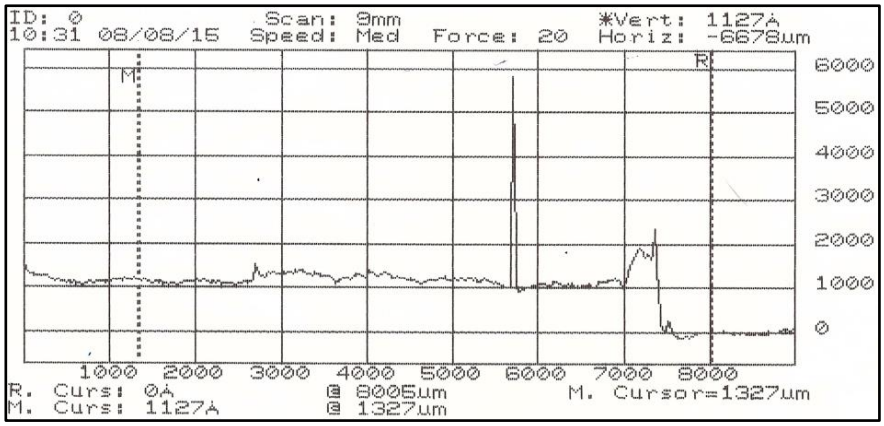

Figure 3.6 Thickness measurement of sample 5 is 113nm

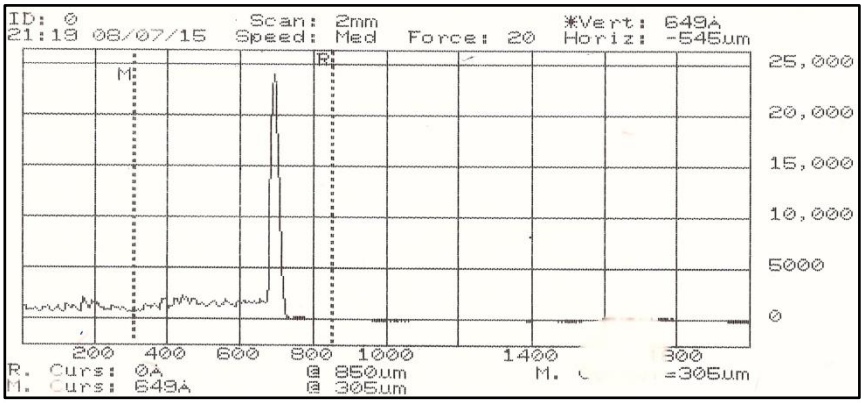

Figure 3.7 Thickness measurement of sample 5 is 65nm

The thickness versus concentration of nano silica concentration is plotted in Figure 3.8. As can be seen, as the concentration for the nano silica increases, its thickness increases.

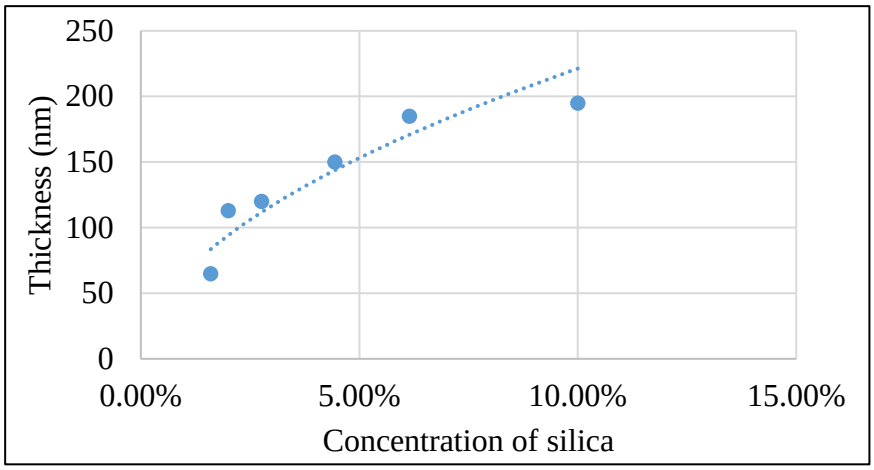

Figure 3.8 Relation between concentration of silica solution and thickness of the coating

The transmittance of the samples is measured and shown in Figure 3.9. Sample 5 shows the highest light transmittance of 94.3%, 95.0%, and 94.3% respectively at wavelength 400nm, 550nm, and 700nm. The glass slide with a 113nm thick silica film transmits nearly 4% more light compared to that of a bare glass with transmittance of 90.5%, 91.3%, and 91.4% respectively at the same wavelengths.

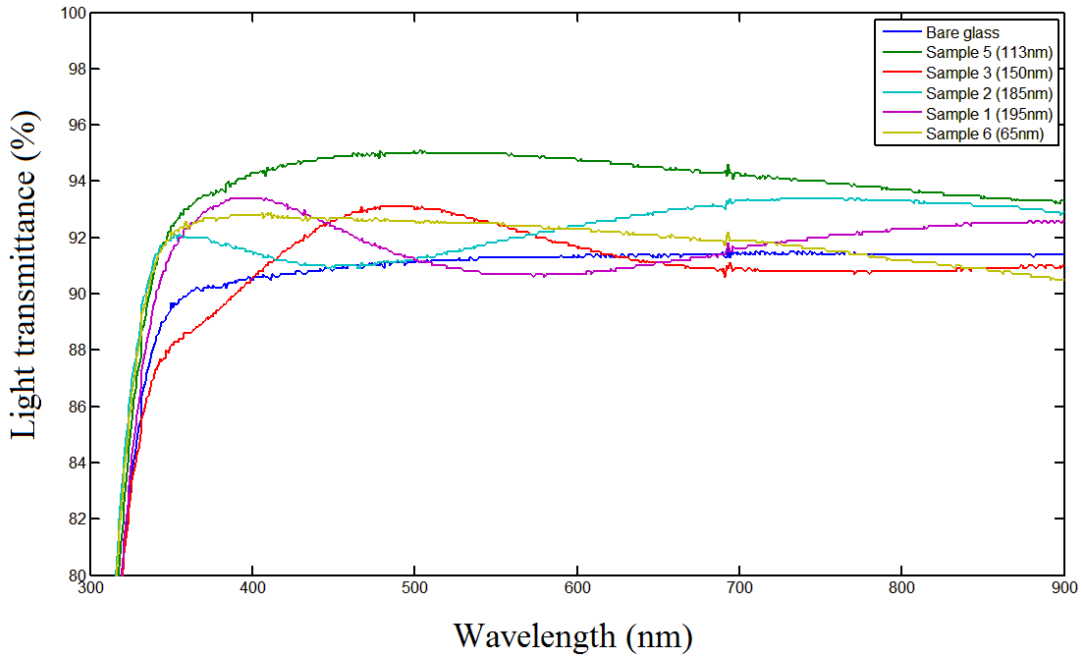

Figure 3.9 Transmittance measurements of the silica films

b) Light Transmittance versus Concentration of Polystyrene Beads

Four samples of polystyrene beads embedded silica coating are prepared. The thickness of these samples is 113 nm which is the optimum thickness found in the last section. The concentration or weight percent of polystyrene beads from sample 1 to sample 4 are 0.125%, 0.25%, 0.5%, and 1%, respectively. The transmittances of these samples are measured and shown in Figure 3.10. The results indicate that from 450nm to 800nm wavelengths, light transmittance raises as the weight percentage of polystyrene increases from 0.125% to 0.5%. After that, the transmittance reduces with further increase of the percentage of the polystyrene beads. This can be explained by the template effect of polystyrene beads. After calcination in air flow at 500 °C, the polystyrene beads are burnt out (the ignition temperature of polystyrene is 488 °C to 496 °C), leaving crater-shaped roughness on the silica surface as shown in Figure 3.11. The roughness is the same size as that of the polystyrene beads. This results in an increase on light transmittance. At low concentrations of polystyrene, increasing its concentration increases the area of the crater-shaped roughness which results in a better light transmittance. As multi-layer of polystyrene beads (mixed with nano silica particles) spread over the entire surface of the glass slides, the relationships between polystyrene concentration and light transmittance change. In a high polystyrene loading silica film, part of the polystyrene beads is buried deeply within the nano silica layer. These polystyrene beads are either not decomposed in the 500 °C thermal process due to the lack of oxygen or there is residual left after burning. In either case, the light transmittance will be affected negatively.

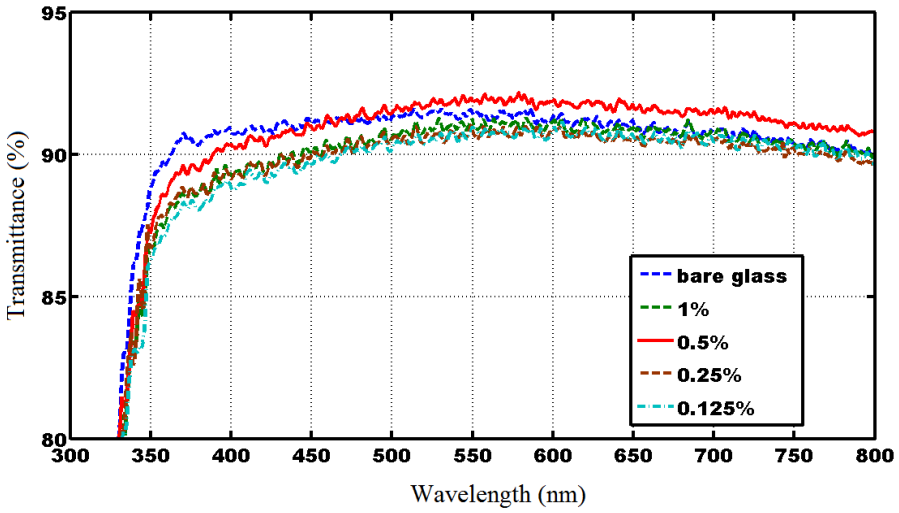

Figure 3.10 Light transmittance of the coating as a function of polystyrene concentration. [3.1]

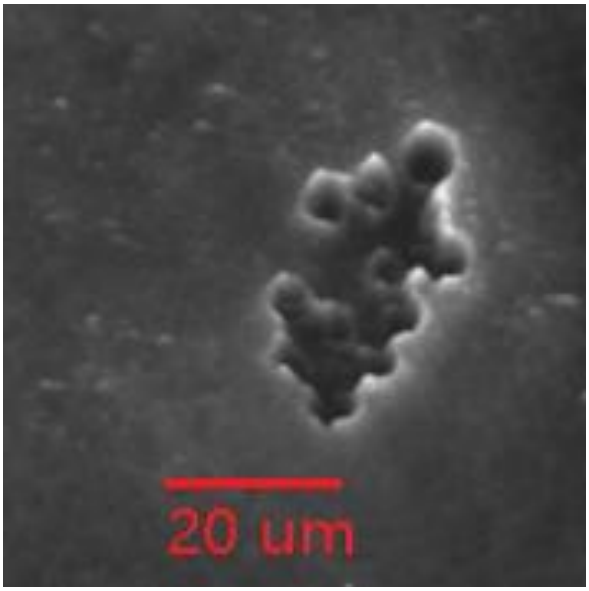

Figure 3.11 AFM image of the silica coating after calcination

c) Water Contact Angle versus Growing Time of SAM Layer

Five samples are prepared with the same silica coating thickness (113nm) and same concentration of polystyrene in the solution (0.5%). However, the growing time of the SAM layers on the 5 samples varies as 0, 6, 12, 17, and 20 minutes. The water contact angle is measured as shown in Figure 3.12 and plotted in Figure 3.13.

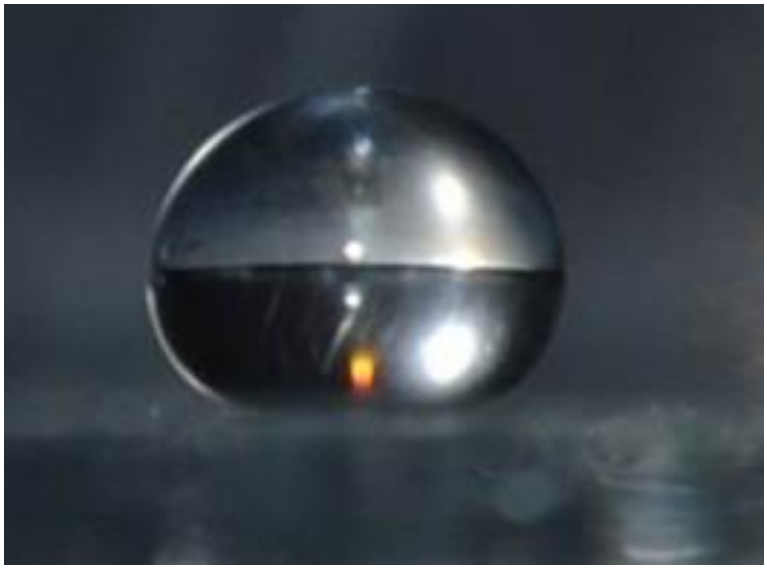

Figure 3.12 A water droplet sits on a silica base hydrophobic surface

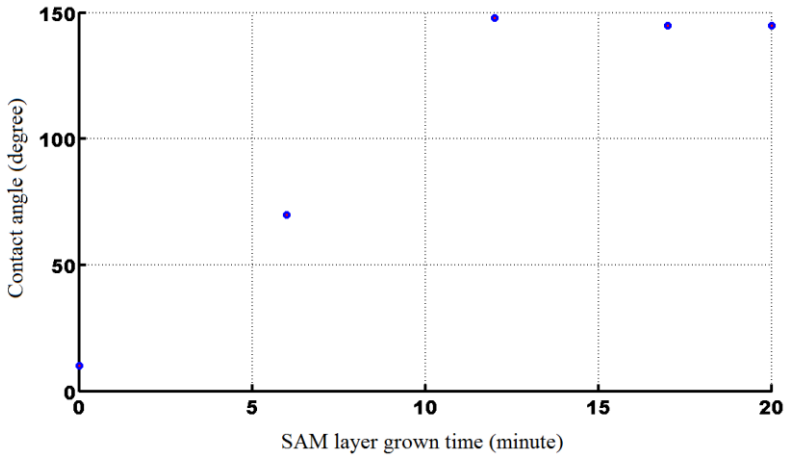

Figure 3.13 Relations between water contact angle and SAM growing time. [3.1]

Figure 3.13 shows that the water contact angle increases with the SAM growing time. At 12 minutes, the WCA reaches the peak value of around 150 degrees. After 12 minutes, the WCA decreases slightly. These results indicate that it takes about 12 minutes for the tridecafluoro-1,1,2,2,-tetrahydro-octyltrichlorosilane molecules to build up the silicon oxygen bond with nano silica particles covering the coating surface. After the coverage is complete, the WCA will not increase anymore.

d) Light Transmittance versus Growing Time of SAM Layer

The light transmittance of the 5 samples in the last section are determined and plotted in Figure 3.14. The plots show that in the first 17 minutes of growing of SAM layer, the light transmittance does not change much. At minute 12, the light transmittance increases slightly. However, at 20 minutes, the light transmittance dropped by about 3%-4%. This is because after 12 minutes' process, a uniform mono molecular layer has been deposited on the silica surface, extending the processing time allows more molecule start to unnecessarily accumulate on the surface and in the solution in a random orientation, this accumulation blocks light. The change of the chemical reaction can be also observed by the color of the solution. In the first 15 minutes, the solution is transparent, after that, it quickly turns into semi-milky in two minutes.

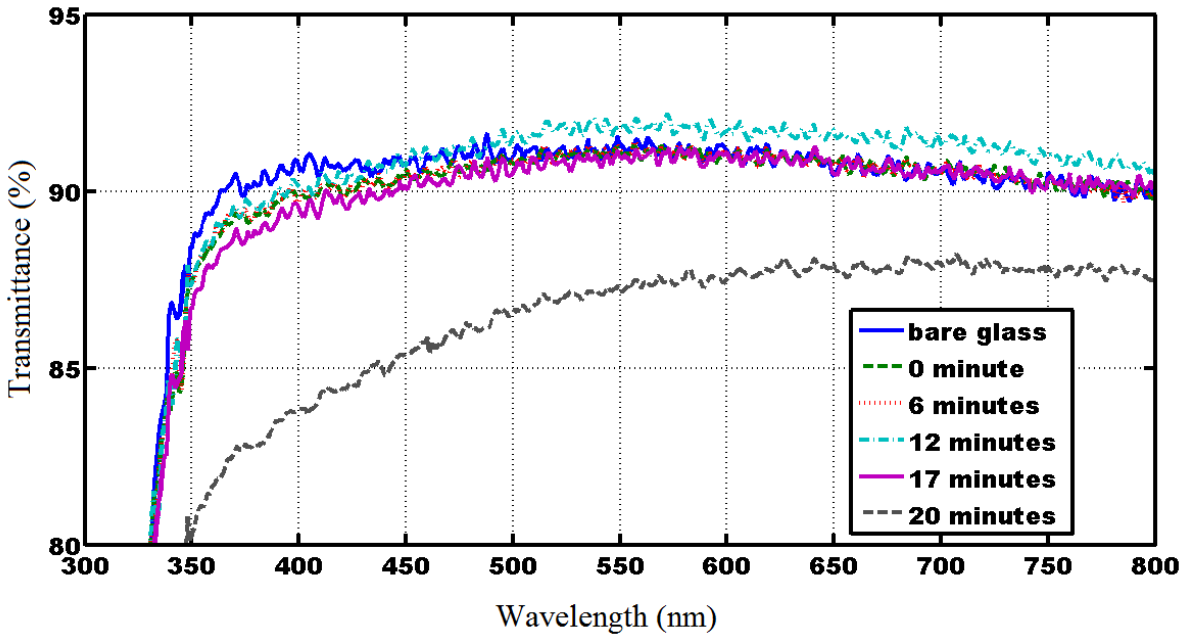

Figure 3.14 Light transmittance as a function of growing time of SAM layer. [3.1]

e) Water Contact Angle versus Growing Time of SAM Layer

Four samples with similar thickness of silica layer, same growing time for the SAM layer but different concentrations of the polystyrene beads in the silica/polystyrene solution are prepared. Results are plotted to investigate how the concentration of polystyrene in the silica affects the WAC of the coating. Figure 3.15 shows the WCA increases from 125° to 150° as the polystyrene bead concentration increases from 0.125% to 0.5%. At the concentration of 1%, the water contact angle decreases. Figure 3.14 reveals that the increase of the polystyrene loading enhances the surface roughness at the beginning, then after a point, adding more polystyrene will not help to roughen the surface but rather it may even make it smooth.

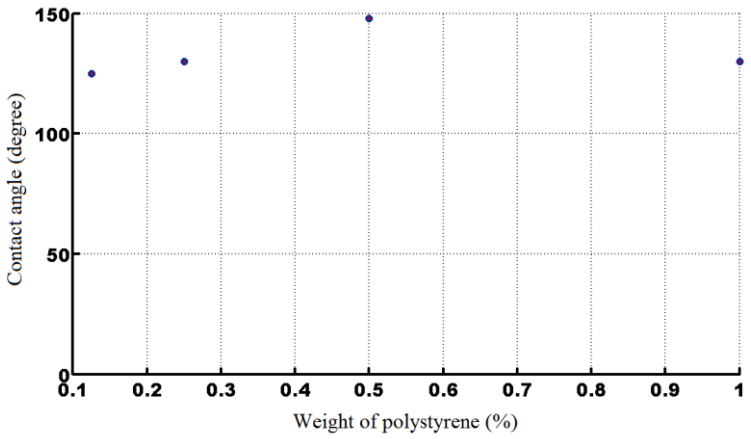

Figure 3.15 Water contact angle as a function of concentration of polystyrene. [3.1]

f) A Test on the Self-Cleaning Efficiency of the Coating.

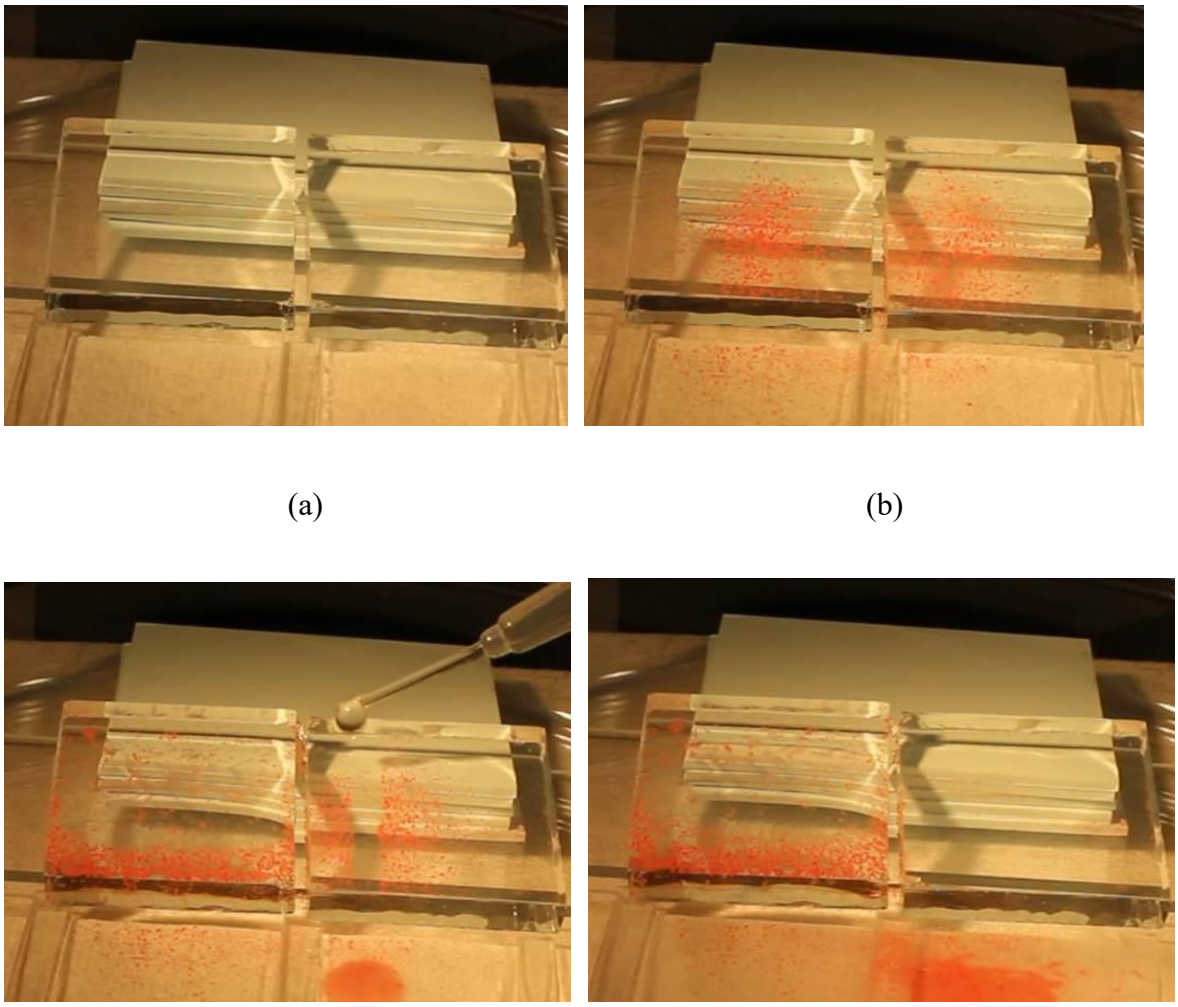

(a) (b)

(c) (d)

Figure 3.16 Demonstration of a self-cleaning surface

In Figure 3.16, self-cleaning efficiency of two glass samples are tested. The glass sample on the left is a normal glass, cleaned with a piranha solution, the right glass is coated with the silica hydrophobic layer. In Figure 3.16(b), same amount of red dusts are sprinkled on both slides. Water drops are dripped onto the two slides as shown in Figure 3.16 (c). On the left glass, water mixed with the particles and stuck onto the glass surface; while on the right, water drops rolled away with particles. As shown in Figure 3.16 (d), the silica hydrophobic glass on the right is perfectly cleaned while the normal glass shown in Figure 3.16 (d) still

has red particles remaining on it.

3.1.4 Reliability Test of Silica Based Hydrophobic/Anti-Reflective Coating

a) Abrasion Test

The test method used is MIL-STD-810G, and an Ecomet 4 variable speed grinder-polisher is used for carrying out the test. In the test setup (Figure 3.17), a felt covered disc is connected to a rotor, and apply abrasion force on to the sample, which is placed on top of the felt surface. The coated side of the glass sample faces down, the upper side of the glass is glued onto an aluminum sample holder, which connects to the pressure head. In the test, the pressure exerted on the sample is 1.9×10^4 N/m^2. The total stroke length in the test is 60 meters.

After the abrasion test, the sample is cleaned in ethanol and DI water orderly. After that, the light transmittance and water contact angles of the samples are examined.

No light transmittance decrease is observed. The water contact angle decrease is less than 5%.

Figure 3.17 Abrasion test setup

b) UV Test

UV radiation test is carried out in a closed chamber with a Spectroline X-series UV bench and lamps (UVA). The radiation intensity of the UVA on the surface of samples is measured to be 2.7Mw/cm^2 by a UV light meter (Spec scientific UVA/B light meter 850009). The test lasts for 1000 hours.

The water contact angle and light transmittance are measured afterwards. No degradation on transmittance or WCA is observed.

c) Temperature Cycling Test

A test chamber (Delta 9023) is used to provide a cycling temperature in the test, from -45°C to 120°C. The chamber connects to a liquid nitrogen tank as a cooling source (Figure 3.18), and uses heater strips to heat up the inner environment and the samples. When the setting

temperature reached the maximum or the minimum, it stays still for 5 minutes to soak up the sample. It takes 28 minutes to complete one cycle, and in the test, 100 cycles are completed.

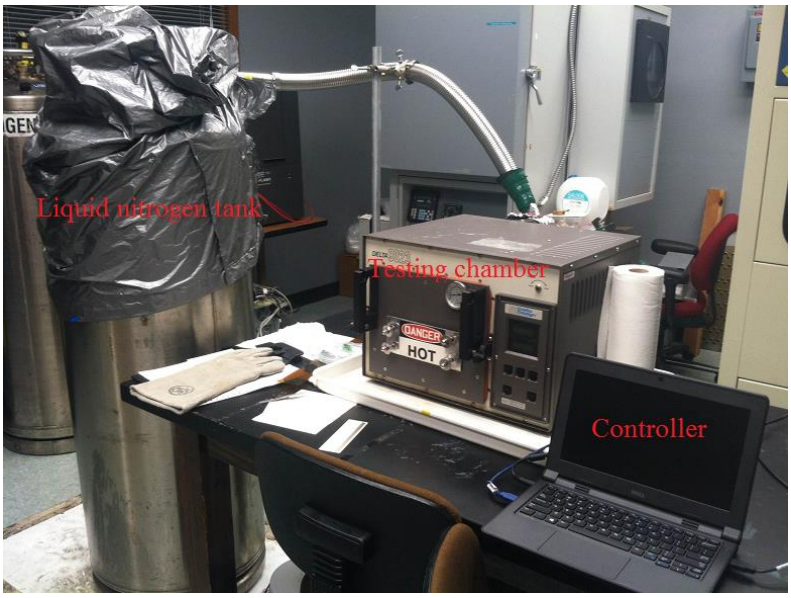

Figure 3.18 Temperature cycling test setup

The WCA and light transmittance measurements show no change on the thermal cycling processed samples.

d) Heat Test

The samples are placed in an furnace (Cole-Parmer 750-14) set to 200°C for 500 hours. No degradation on light transmittance or WCA is observed.

3.2 Polymer Based Anti-Reflective/Hydrophobic Surface using Nano Imprinting Technology

In the section 3.1, a bottom-up approach is utilized to grow nano structures on substrate. A bottom-up synthesis method implies that the nano structures are fabricated by adding atoms on a substrate. In this section, a top-down approach is used to create nano surface

configurations. In the top-down approach, atoms are etched out of the substrate to form nano structures.

3.2.1 Preparation of Polymer Based Anti-Reflective & Hydrophobic Surface.

There are two major procedures to prepare a polymer based anti-reflective and hydrophobic surface. The first step is to use silicon etching method to create the desired configurations on a silicon wafer. The second step is to transfer the patterns on the silicon wafer on to transparent polymer thin films using a nanoimprinting method.

Specifically, in the first procedure, silicon substrate is first patterned using photo lithography as shown in Figure 3.19 (a). Then a deep reactive-ion etching is performed to etch down vertically to create pillars as shown in Figure 3.19 (b). After that, an isotropic etching process is carried out to taper off the pillar as shown in Figure 3.19 (c) which makes the configuration more desirable in terms of light transmittance based on the simulation performed in Chapter two.

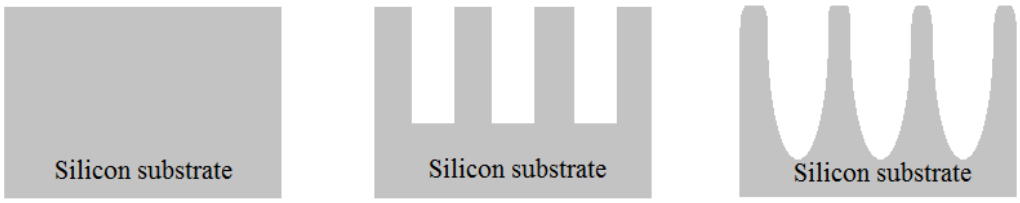

Figure 3.19 Silicon patterning process

a) Designing Mask for the Photolithography Process.

The mask design is shown in Figure 3.20 (a), (b), and (c).

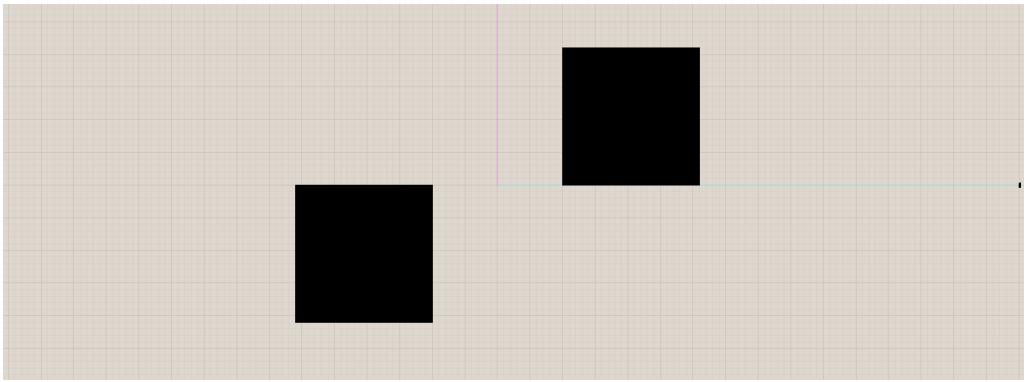

(a)

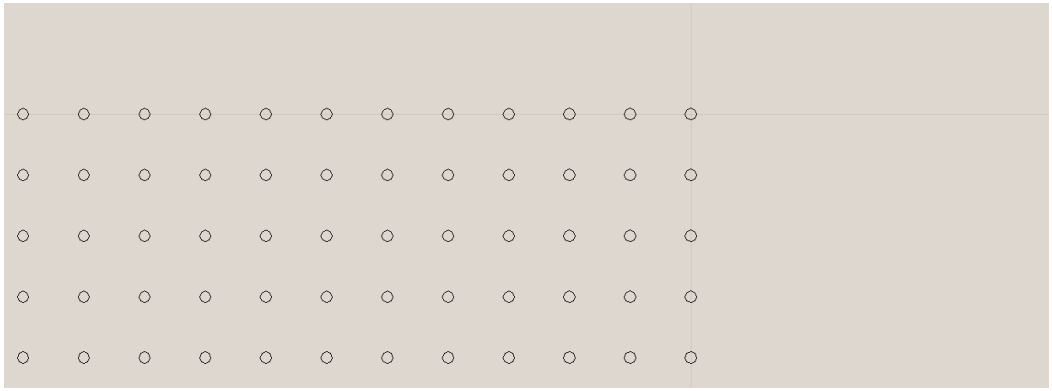

(b)

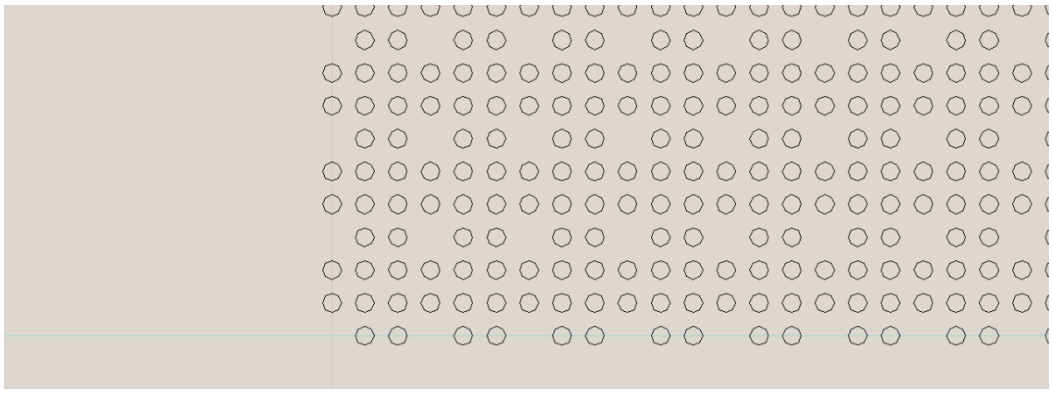

(c)

Figure 3.20 Mask design

Two big square blocks are designed on the mask as shown Figure 3.20 (a) with dimensions of 10 mm by 10mm. The left block consists of circles with diameters of 2 microns. The right block is built up by the same circles, with some of them removed. The space between two circles in the Figure 3.20 (c) is 1.5μm. Figure 3.20 (b) and (c) are complementary to

each other, that is, if Figure 3.20 (a) rotates around the origin for 180°, it fills up all the removed circles in Figure 3.20 (c). There are two alignment markers on the two sides of the mask. This design was to enable a two-layer photo lithography process to realize a hydrophobic and anti-reflective rough surface. However, due to low resolution of the exposer, the alignment between two layers cannot be achieved. So the two block in the mask, Figure 3.20 (a) and (b) are used as single layer masks, respectively. A quartz photomask is fabricated for this purpose.

b) Photo Lithography

In this process, photo resist with patterns will be coated onto silicon wafer. First, a silicon wafer is cleaned in DI water and dried in nitrogen for 3 minutes, respectively. Then hexamethyldisilazane (HMDS) is coated onto the cleaned wafer in a spin coating system (6800 Spin Coater Series, Specialty Coating Systems) to enhance the adhesion between silicon wafer and photo resist, which is coated next. The AZ 4110 photo resist is spin coated at 5000rpm to form a one micron thick layer on the wafer. After coating, the wafer is baked on a hot plate at 110^{o}C for 110 seconds. This baking process solidifies the photo resist and removes the solvent. A well-coated silicon wafer has a uniform green color. After the baking process, the wafer is cooled down and then exposed in an exposing system (Suss Microtec MA150 Contact aligner). The expose time is 17 seconds with the 65 μm gap between the photomask and wafer.

In the next step, the exposed wafer is emerged in a developer (AZ 300 MIF) for approximately 150 seconds to remove the unwanted photoresist. Then the wafer is removed

from this developer solution, rinsed in DI water and dried. Lastly, the wafer is examined under a microscope. Figure 3.21 (a) shows the resultant photoresist patterned by the mask block on the left and Figure 3.21 (b) shows the resultant photoresist patterned by the mask block on the right.

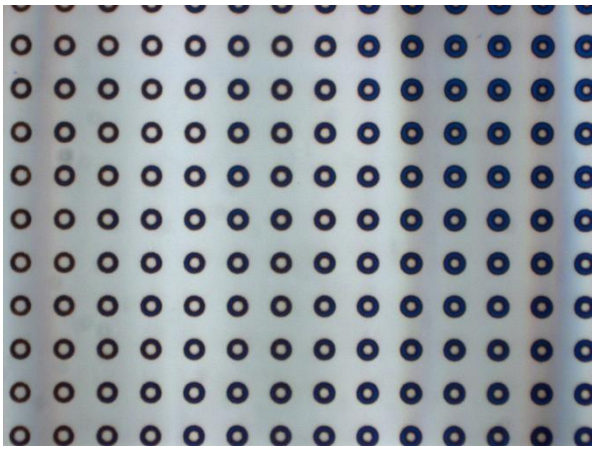

(a)

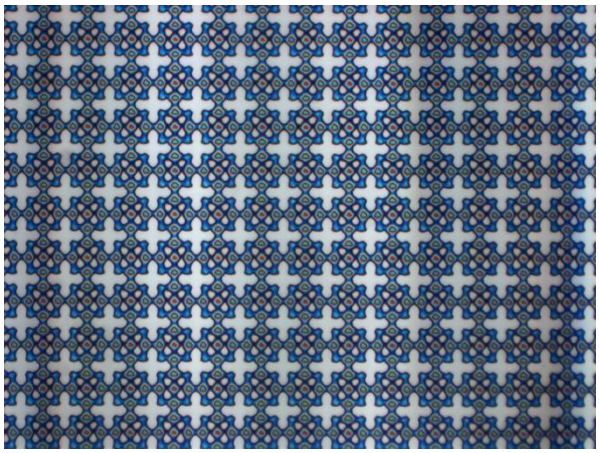

(b)

Figure 3.21 Microscopic image of photo resist on silicon wafer

c) Anisotropic Etching

The anisotropic etching is processed on a deep reactive ion etch (DRIE) system. This reactive ion etch utilizes sulfur hexafluoride (SF_6) and O_2 to etch off the silicon that is not

protected by the masking mask. This DRIE recipe includes two procedures, one is the etch off of the silicon to build vertical wells in the silicon, and the other procedure is to use octafluorocyclobutane (C_4F_8) gas to passivate the side walls of the wells after every several seconds of etching to prevent side wall from being bombarded by the plasma. Because of this protection, the side wall is vertical and the aspect ratio is high.

Considering this reactive ion etch has a high etch selectivity (larger than 300) over silicon and silicon dioxide, the thermal oxide layer on the wafer surface is used as etching mask. Thus, before DRIE process, both the samples with photoresist pattern indicated as Figs. 3.19 (a) and (b) (the two samples are numbered as sample (a) and sample (b)) are etched in buffered oxide etching (BOE) solution to remove the unwanted oxide layer. As a result, part of the silicon is exposed, and ready to be removed in the next etching process. After BOE etching, sample (a) is processed in DRIE system for approximately 2 minutes. The recipe of the etching is shown in Table 3.3.

Table 3.3 Recipe of deep reactive ion etch

Step	Cycles (#)	Time (sec)	SF_6 flow (sccm)	O_2 flow (sccm)	C_4F_8 flow (sccm)	Coil Power (W)	Platen Power (W)
Etch	5	12	150	15	0	650	12
Passivate	5	5	0	0	95	650	0

Sample (b) is etched in a reactive ion etch (RIE) system.

The recipe is indicated in Table 3.4.

Table 3.4 Recipe of reactive ion etch

Step	O_2 flow (sccm)	SF_6 flow (sccm)	Pres. (mTorr)	Power (W)	Time (Min:Sec)
Etch	13	112	275	325	5:00
Stability	13	112	275	0	0:10

After DRIE and RIE processes, samples (a) and (b) are examined in scanning electron microscope and atomic-force microscopy (AFM), respectively. Figure 3.20 shows the SEM of the DRIE etched sample. The etched features have consistent shape and dimensions. They also have consistent depth. Figure 3.23 shows the AFM photo of sample (b). As can be seen, the features are very consistent and are similar to those shown in the SEM photo of Figure 3.22.

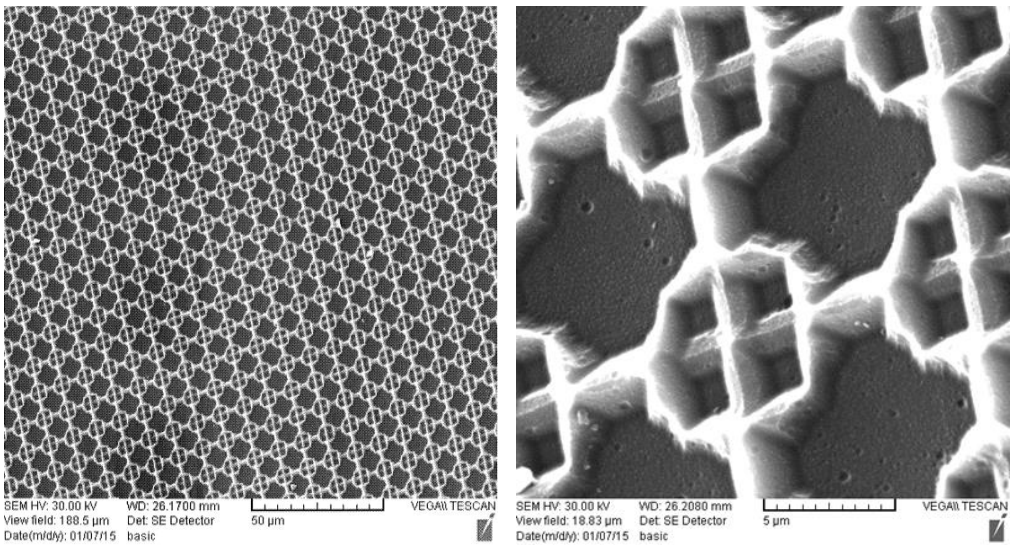

Figure 3.22 SEM image of sample (a)

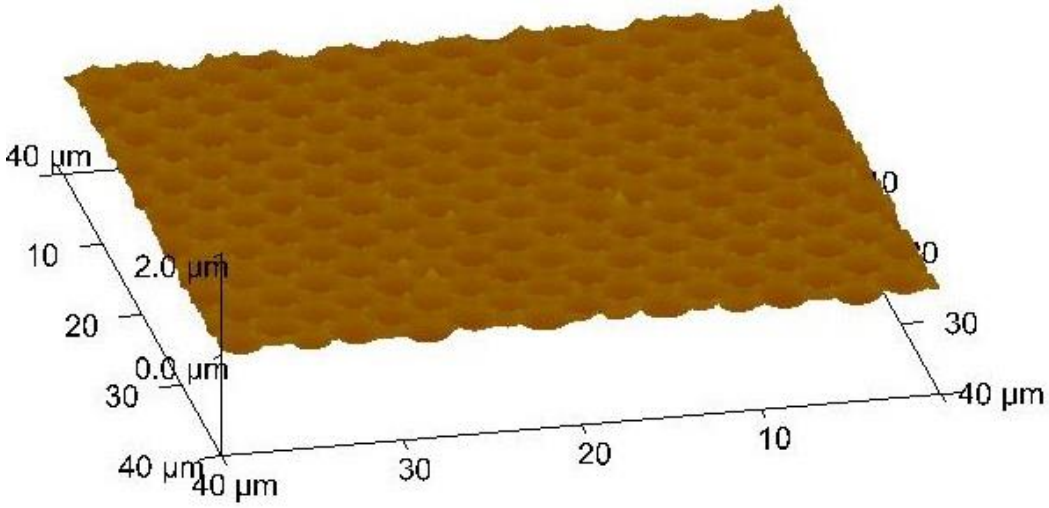

Figure 3.23 AFM image of sample (b)

d) Isotropic Etching

The two samples are etched in a HF/Nitric/Acetic Acid (HNA) solution. The solution consists of 110 mL acetic acid (>98%), 70 mL nitric acid (70%), and 40 mL hydrofluoric acid (49%). The etching process is complete in a Teflon container in a fume hood. Etching time is controlled to be 55 seconds. After the etching process, the wafer is rinsed in DI water for 3 minutes. The sample is scanned in a SEM, and the image is shown in Figure 3.24. The unique features created after the HNA etching can be clearly shown in Figure 3.24. Figure 3.25 shows the AFM photo of the similar sample after HNA etching. As can be seen, unique sharp features are clearly seen in these AFM photos.

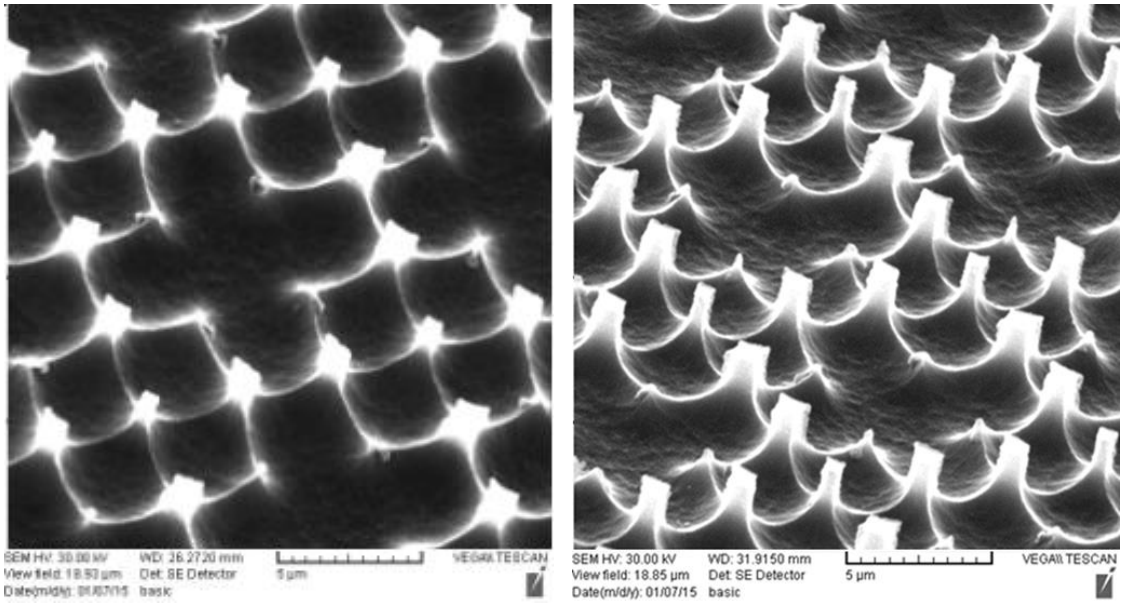

Figure 3.24 SEM image of sample (a) after HNA etching (the sample on the left image is 40° tilt, and on the right 60° tilt)

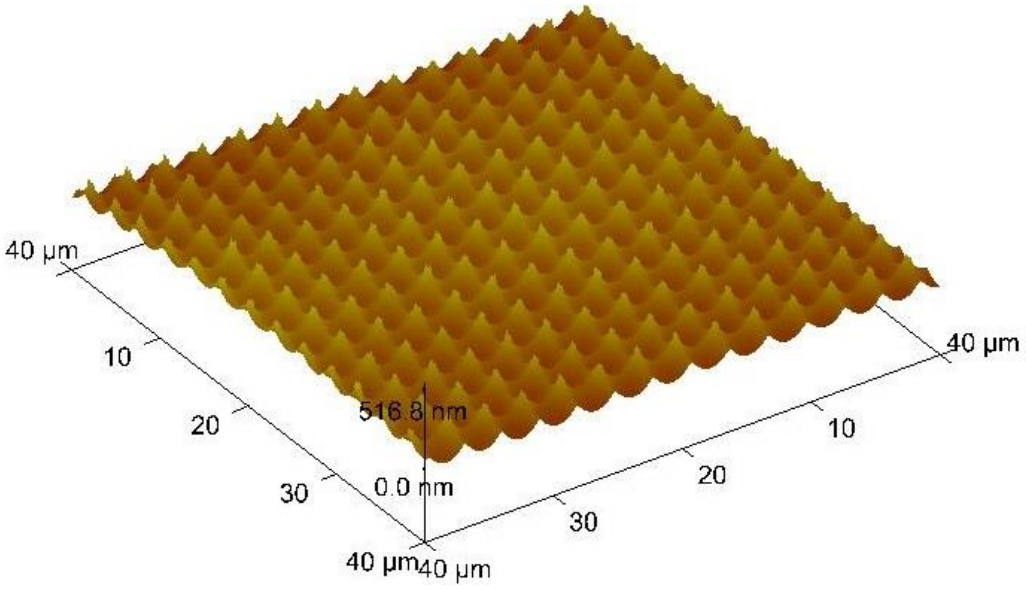

Figure 3.25 AFM image of sample (b) after HNA etching

e) Nanoimprinting Process

In a typical nanoimprinting process, substrate, moldable material, and mold are the basic elements. In this nanoimprinting step, the etched silicon samples (a), and (b) are used as mold, glass slides are the substrate, and silicone elastomer (silicone elastomer R-2187, purchased from Silicon Technology) is used as the moldable layer. There are several properties that this silicone elastomer possesses that make the material a good candidate moldable layer, such as high light transmittance, easy cure process, and chemical stability. Figure 3.26 shows the process steps for the nanoimprinting process.

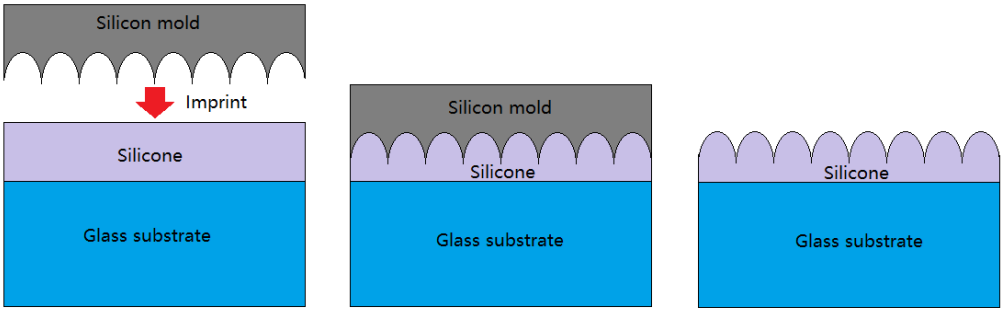

Figure 3.26 Sketch of nanoimprinting process

To transfer the patterns from the etched silicon samples onto glass substrates, the first step is to coat the silicone on the glass slides. Glass slides are first cleaned with acetone, IPA, and DI water for 15 minutes, then dried in nitrogen. Silicone elastomer part A and part B are mixed with the ratio of 1:10, the mixture is stirred with a glass bar for 5 minutes. After mixing, the silicone is placed in a centrifuge and spin at 4000 rpm for 30 minutes to remove the bubbles induced during stirring. All the processes need to be well planned and prepared, so they can be completed as quickly as possible. Because the work time for silicone is three hours after mixing, the mixture becomes more viscous every minute passes.

The second step is coating the silicone onto the cleaned glass slides. Spin rate is set at 8000 rpm to form a layer of silicone with the thickness of about 10 microns. After coating, the samples are placed in a refrigerator (-15°C) for 30 minutes to let the silicone self-level to the surface. The low temperature prevents curing while allowing the silicone to level over the surface.

The next step is nanoimprinting. A mold release is first sprayed onto the silicone samples (a) and (b). After 5 minutes, sample (a) and (b) are placed on the glass slides, with the patterned surface of silicon facing the silicone side. The two stacks are put in a vacuum oven, with a 100g weight on each of the samples to apply pressure when curing. The oven is set at 150°C at 5 KPa pressure. The curing process lasts for 15 minutes.

At last, samples are removed from the oven. After samples cooling down to the room temperature, silicon molds are removed from the glass slides. Glass slides are cleaned in

acetone, IPA, and DI water to remove mold release residual.

The sample prepared using the DRIE yielded the tallest roughness on its surface. In the nanoimprinting surface, the cured silicone was not peeled off as expected, and the residual contaminated the silicon sample (a). In the next section, tests are made only on the samples that prepared from RIE etching.

3.2.2 Measurement of the Samples and Discussions

Sample (a) is measured with an AFM system and the surface feature is plotted in Figure 3.27. From the image, we can see that the period of the roughness is approximately 3 microns, with a height of about 0.5 micron.

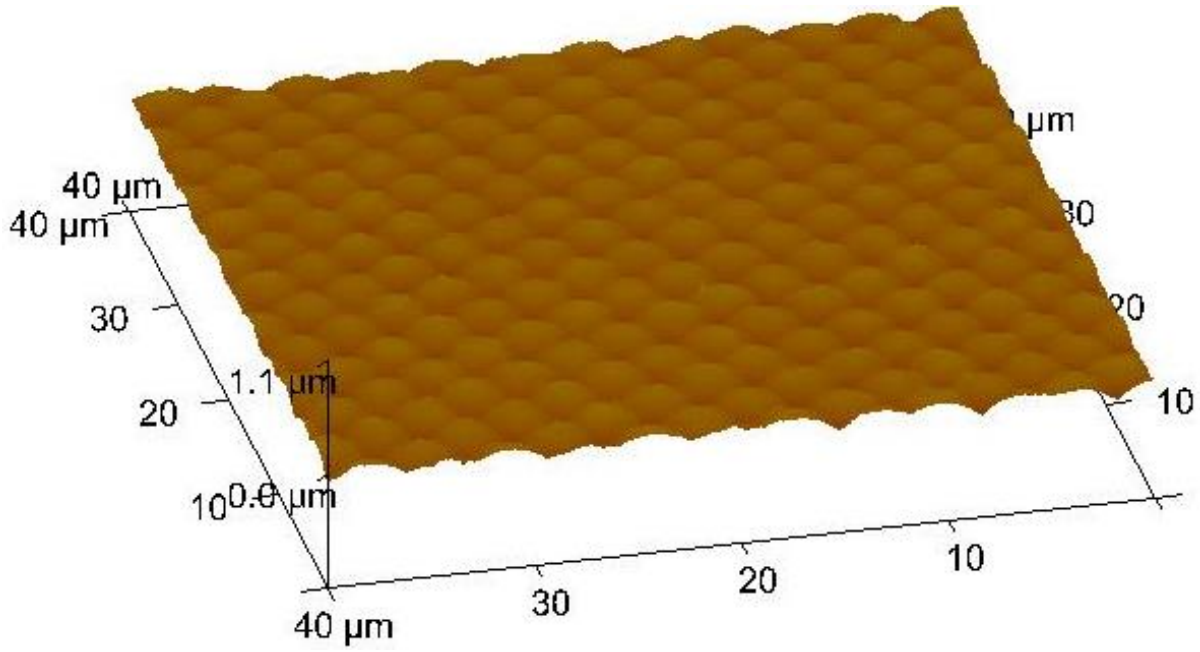

Figure 3.27 AFM image of the nanoimprinting processed silicone surface

The light transmittance of this silicone coated sample is 93% at 550 nm wavelength. That is 1.5% higher than the bare glass slides. Compared with the silica coated glass sample, the

transmittance enhancement is not so much. That is due to the stronger reflectance at the silicone/glass interface than that at the silica/glass interface.

3.3 References

[3.1] Xingeng Yang, Simon S. Ang, "A hydrophobic/Anti-reflective coating and a nano particle ethylene-vinyl acetate encapsulation for solar cell packaging". Advancing Microelectronics, Nov/Dec 2012

[3.2] M.D. Tyona, "A theoritical study on spin coating technique", Advances in Materials Research, Vol. 2, No. 4 (2013) 195-208

Chapter 4. Nano Particle Embedded Ethylene-Vinyl Acetate Encapsulation

4.1 Introduction of Ethylene-Vinyl Acetate Copolymer

Ethylene-Vinyl Acetate (EVA) is also known as poly (Ethylene-Vinyl Acetate). It is a copolymer synthesized from two monomers of ethylene and vinyl acetate as shown in Figure 4.1. EVA was first patented by DuPont in 1956. Due to its desirable mechanical, chemical, and optical properties, it has been used as an encapsulation for solar cells in photovoltaic panels for decades.

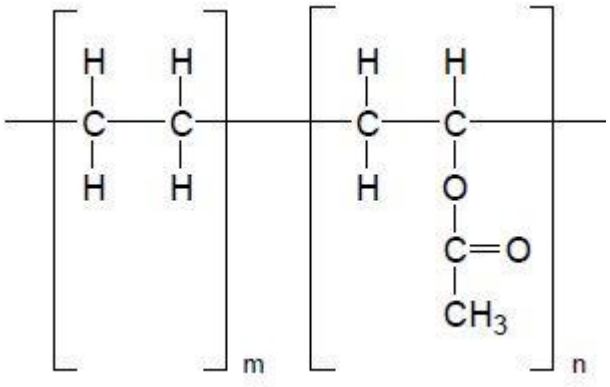

Figure 4.1 Ethylene-Vinyl Acetate copolymer

With different portions of vinyl acetate, the copolymer exhibits diverse physical appearance and properties. At low concentration of vinyl acetate, EVA is similar to a low-density polythene due to its high crystallization of ethylene, which is stiff and relatively fragile. With increase of vinyl acetate concentration of vinyl acetate, crystallization reduces and the copolymer becomes flexible similar to rubber. Most of the EVA used for solar cell encapsulation has a vinyl acetate weight percent from 10% to 50% [4.1,4.2]. In general, EVA with this range of vinyl acetate weight percentage exhibits excellent light transmittance, good thermal properties, and toughness. EVA with a lower than 10% vinyl acetate weight percentage is normally considered as an acetate modified polyethylene while those with higher than 50% vinyl acetate are referred to as ethylene vinyl acetate rubber. In this dissertation work, we only investigate EVA for solar cell encapsulation in photovoltaic (PV) panels.

4.2 EVA Degradation in Solar Cell Encapsulation

Although EVA encapsulation is relatively chemically stable, it degrades under ultra violet

radiation, extreme heat, and humidity environment.

In the later 1980s, yellowing or browning problems were observed on the EVA encapsulations for solar cells as shown in Figure 4.2 [4.3-4.5]. As the EVA turning yellow or brown, its light transmittance drops dramatically which reduce the overall efficiency of solar energy conversion in solar cells. From 1986 to 1990, the annual power output at the Carrisa photovoltaic (PV) power plant in California dropped by more than 45% due to EVA browning as shown in Figure 4.3 [4.6].

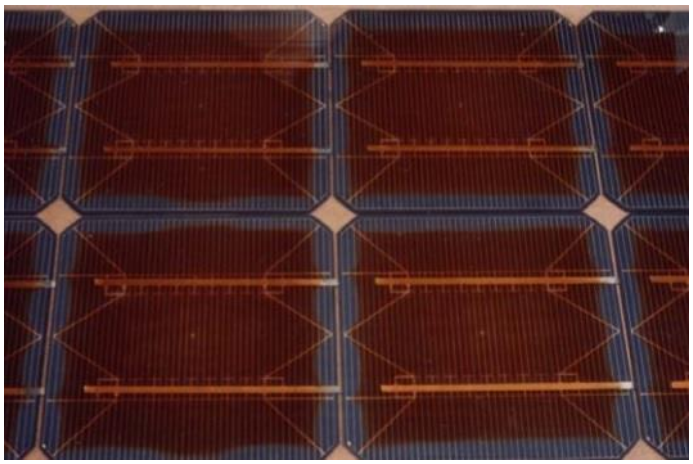

Figure 4.2 Browning of EVA encapsulation [4.5]

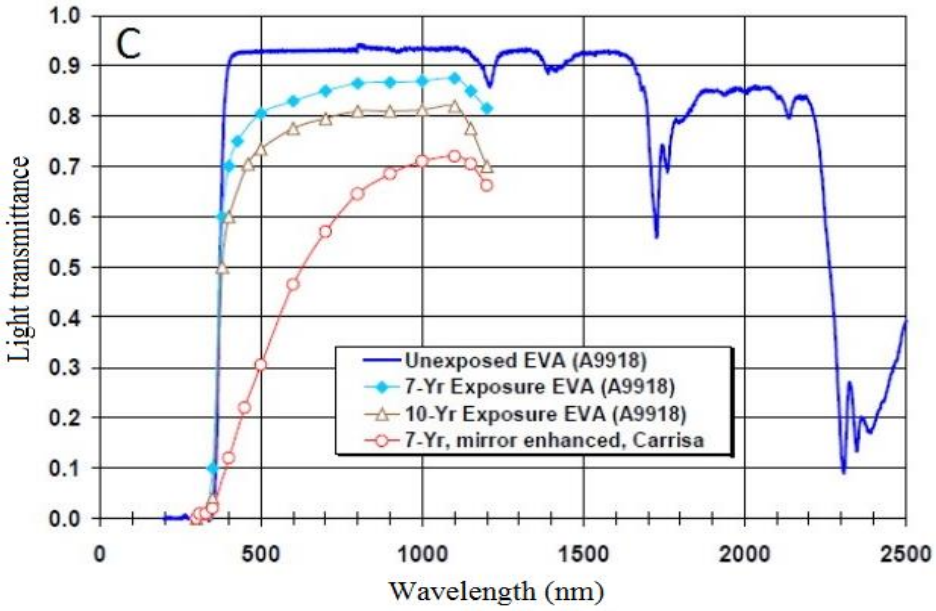

Figure 4.3 EVA transmittance degradation [4.6]

Besides degradation of light transmittance, the yellowing of EVA also decreases its adhesion strength with the top glass panel and the solar cells. This may accelerate the degradation of solar cells due to the lack of physical protection and even may lead to a mechanical failure of the PV panel. To address the yellowing or browning problem, many researchers studied the mechanisms behind this phenomenon and proposed solutions to reduce or eliminate the degradation of the EVA copolymer.

In Pern's work [4.7], the degradation of EVA is attributed to "free radicals" which were mainly generated by UV radiation in combination of oxygen. These "free radicals" migrate into the copolymer matrix, severe the cross-linked polymer network into smaller molecules, and generate aldehyde and acetic acid to cause the degradation [4.7]. Other research groups [4.8] also proposed similar explanation of EVA degradation. To reduce and mitigate this degradation mechanism, UV absorbers that reduce the UV radiation by decreasing the

generation of free radicals, UV stabilizers that react with free radicals generated by UV radiation, and antioxidant which chemically reduce the oxidation process are added into the EVA copolymers. These additives have been shown to efficiently prolonging the lifespan of EVA in solar cell encapsulation over the years.

However, the demand for more durable PV panel never ended. In this work, a new approach to further reduce the UV degradation based on the nano particle embedding into the EVA copolymer is investigated. The objective of embedding nano particles into the EVA copolymer is to restrict “free radicals” and oxygen in a small localized area, hence stopping them from propagating into the copolymer matrix.

4.3 Gas/Particle Diffusion in Polymers

Both the “free radicals” and the oxygen gas follows similar manner to propagate in the EVA. Two major factors influence diffusion rate [4.9]. First, there must be holes available in the polymers. In a diffusion process, a hole is filled up by impurities, and at the same time another hole is created at the adjacent location, which is previously occupied by the impurities. The newly created holes could be filled up later by polymer molecules or other impurities. Second, a continuous path through the polymer is present in the polymer matrix. This means that the relocation of the holes and impurities should be continuous and lasts for a long-time span. Thus, in macroscopic view, impurities diffuse in the matrix and change its composition along its path.

All polymers have voids due to their molecular structures. The only way to change the gas

or particle diffusion is to add microscopic particles into the polymer to form a barrier. These barrier particles will cut off the path along which gases and particles propagate. In this blocking process, particle dimensions play a crucial role.

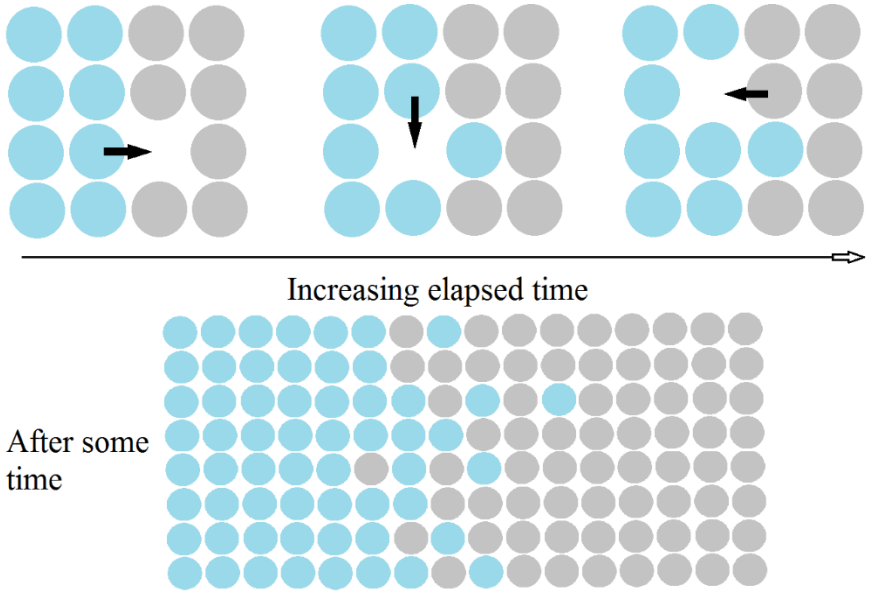

Figure 4.4 Sketch of diffusion mechanism in polymer [4.9]

Cui el al [4.10] studied the modeling of barrier properties in nanocomposites. With the existence of embedded fillings, the gas or particles have to travel along a longer and more torturous path when displace from point A to point B in a given direction, specifically vertically from the top side to the bottom side of the polymer. This torturous path results in a reduced diffusion thickness. Cui el. al. [4.10] further explained that the diffusion rate is positively correlated with the width of the filling particle (W) and distance between adjacent particles (D), and negtively correlated with the side length of the particles (L) as shown in Figure 4.5.

where D is a parameter that relates to the loading of the filling particles, L and W are the

factors determined only by the particle dimension. According to this model, particles with relatively big area but small thickness are preferred when a reduced diffusion is desired.

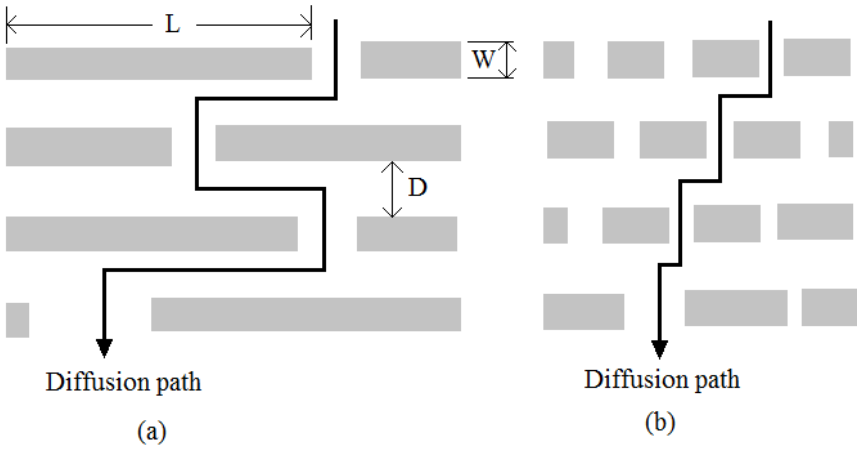

Figure 4.5 Tortures diffusion pathway in a nanocomposite [4.10].

4.4 Nano Diamonds Embedded EVA Encapsulation

4.4.1 Nano Diamond Nanoparticles

Nano diamonds are relatively inexpensive material. They possess special mechanical, optical, thermal, and magnetic properties due to their nano size and large surface to volume ratio. Nano-composites involving nano diamond particles have been studied [4.11-4.13]. The property enhancement of these nano diamond nano-composites, compared with a pure matrix, in terms of mechanical strength, adhesion strength, thermal conductivity, degradation, refractive index is reported in many literatures [4.11-4.13]. However, there is no reported work on nano diamond EVA composite. This work reports on the preparation and characterization of the nano diamond EVA composite for the encapsulation of solar cells.

4.4.2 Functionalization of ND

Although nano diamond reveals diverse advantages in preparing a functional composite, commercial nano diamonds are seldom directly used in practice due to the impurities and agglomeration which will considerably change the properties of NDs. There are metal residuals and agraphitic carbon surround the NDs cores, as well as varied chemical groups. By removing these impurities and groups, NDs can be “purified” to obtain their desired quality. Most of the industrial ND products are purified in liquids oxidants to remove non-diamond carbon and followed by a hydrochloric acid (HCl) clean to wash away non-carbon composites. In this work, an air oxidation method is adopted and followed by an HCl clean to achieve the same goal for consideration of environmental impacts [4.14]. Besides purification, there is another pre-treatment needed before NDs can be used to mix with polymers since chemical groups need to attach onto the NDs in order to functionalize them. Different chemical groups will modify NDs properties differently. In general, there are two categories of functional groups: groups that are grafted by a high temperature gas process and groups that are grafted by a solution process [4.14]. Carboxyl (-NH2) group readily reacts with polymers and achievable through a relatively safe solution process is adopted in this work.

4.4.3 Preparation of ND Embedded EVA Encapsulation

a) Purification of NDs and Attachment of –COOH groups

Nano diamond particles are oxidized in air environment in an oven for 5 hours at 425 °C [4.15]. For an evenly oxidation process, these nano diamond particles should be spread

out into a thin layer with a cover to prevent them from being swept away by the strong air flow in the oven. After oxidation, ND particles are cleaned with a 37% hydrochloric acid (HCl) solution for 24 hours and extracted from the solution using a centrifugation process. Following this, these ND particles are further rinsed several times in DI water until a PH value of 5.3 is obtained. Then, ND particles are precipitated using a centrifuge, the excess water is removed with a burette, and then dried in a vacuum oven overnight at 60°C. After these steps, surrounding impurities such as metal, metal oxide and agraphitic carbon, due to the detonation synthesis process, would have been removed to reveal their carbon atoms with –COOH groups connected to them. As such, the surface of the ND particles has been activated and –COOH group has been obtained.

b) –Cl Groups and –NH_2 Groups

Subsequently, the –COOH group is substituted with a –Cl and then the –Cl is replaced with a –NH_2. The activated ND particles (1.5g) are mixed with 50 mL thionyl chloride ($SOCl_2$) and 0.5 mL N, N-dimethylformamide in a flask. The flask is then sealed using a glass stopper and ultra-sonicated for 10 min to disperse the agglomerated ND particles. After this, the flask is connected to a condenser with running chill water. At the other end of the condenser, a desiccating tube is installed to prevent ambient water vapor from entering the reaction flask. The reaction is maintained at 70 °C with constant stirring for 24 hours. Then, thionyl chloride is removed in vacuum at 30°C. The remaining solid particles are rinsed with anhydrous tetrahydrofuran for 5 times, the suspension is left to precipitate ND particles at each rinse. Finally, the NDs-Cl particles are dried in vacuum.

The ND-NH_2 is prepared as follows. One gram of ND-Cl is mixed with 50 mL of anhydrous ethylenenediamine followed by ultra-sonicated. Again, the reaction flask is connected to a condenser with running chill water and the reaction is maintained at 60ºC with constant stirring for 24 hours. After that, the prepared ND-NH_2 is repeatedly washed with THF until the pH paper reveals a neutral pH (pH=7) solvent. This pH test is performed by taking a few drops of THF from the upper surface of the solvent. After mixing with 20mL of DI water, a pH paper is used to check. Then, the cleaned ND-NH_2 is dried in vacuum with desiccant.

c) Preparation of EVA-ND Composite

Two grams of commercial EVA sheets are first dissolved in 10 mL THF solvent, the solution is ultra-sonicated for 30 minutes for a better dissolution. Then 0.1 g ND-COOH NH_2 is dissolved in THF, ultra-sonicated for 10 minutes. The two solutions are then mixed together by stirring and ultra-sonication. In this way, ND particles are embedded into the EVA polymer. The nano-diamond/EVA composite sheet is obtained by vaporizing away the tetrahydrofuran. After this, samples are prepared using a lamination structure of glass-EVA sheet, half of the samples have ND-NH_2 embedded into the EVA sheet and the other half of the samples are pristine EVA sheet for comparison. These samples are cured together in vacuum at 150 °C for 90 minutes to facilitate crosslinking.

Three samples are prepared for adhesion test. Sample one has only EVA film coated on the glass slide. Sample two has an EVA film with 0.4% nano diamonds. Sample three has EVA film with 2.2% weight diamond nanoparticles. The concentration of EVA solid sheet dissolved in the solution remains essentially the same for these 3 samples. These samples

are spun coated and undergone identical curing process.

4.4.4 Characterization

Functionalized ND particles and commercial NDs are mixed with KBr separately and are compressed into pellets, these pellets then are measured using a Fourier transform infrared spectroscopy (FTIR) to verify chemical bonding species. The transmittance of all the samples is first determined using a Cary 500 UV-VIS-NIR spectrophotometer. Their adhesion strength measurements are performed using a Sebastian five adhesion puller.

Metal bars are attached onto EVA surface to prepare for adhesion test on a Sebastian five tester. Before the testing, samples are cured at 150°C for one hour and left at room temperature for 24 hours. From the FTIR test results as shown in (Figure 4.6), a peak around 1580 1/cm indicates the existence of the $–NH_2$ group. The 3200 cm^{-1} peak represents N-H bonding, which further confirms that 1580 peak is due to NH_2 group but not the C=C bonding.

Figure 4.7 shows that ND-NH_2 embedded EVA exhibits approximately 1% increase in light transmittance compared with pristine EVA encapsulation. For pristine EVA encapsulation, the adhesion strength between EVA and glass is 10^6 N/m^2, the measurement between the ND-NH2 embedded EVA and glass slides is $10^7 N/m^2$.

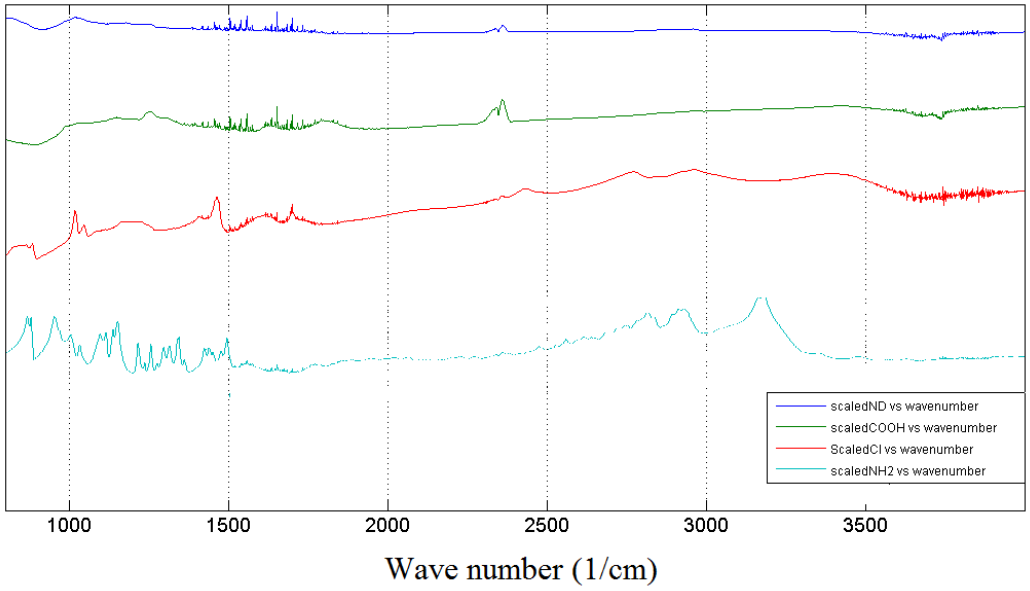

Figure 4.6 Absorption spectrum of ND and functionalized ND

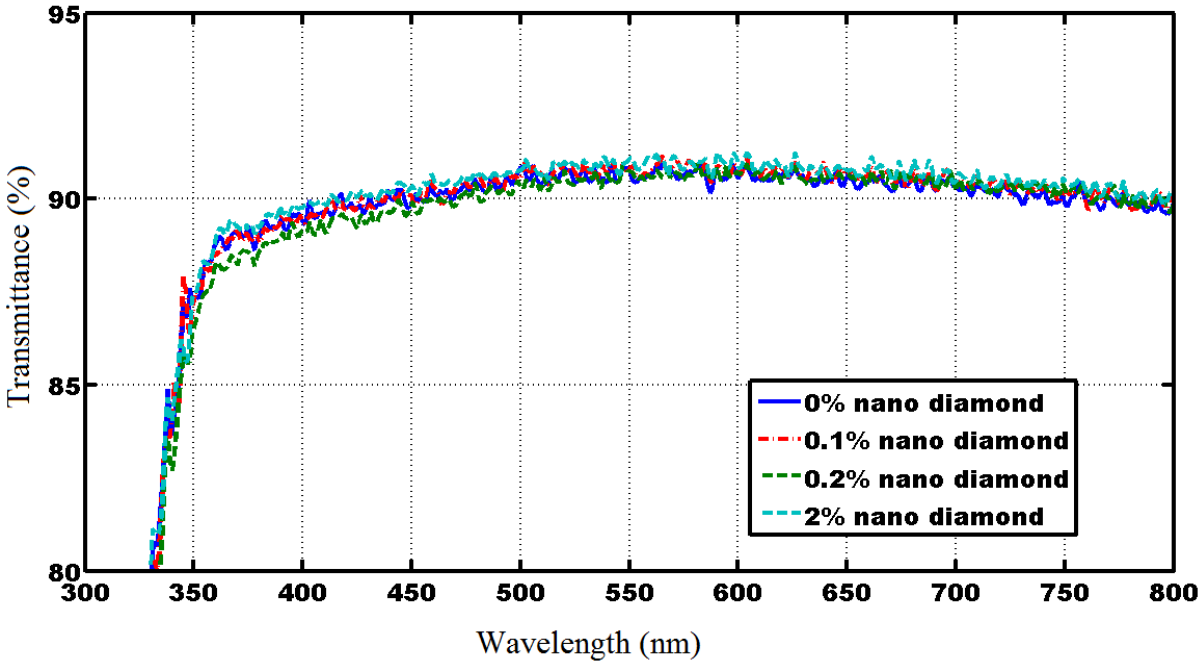

Figure 4.7 Transmittance of EVA and ND embedded EVA sheets

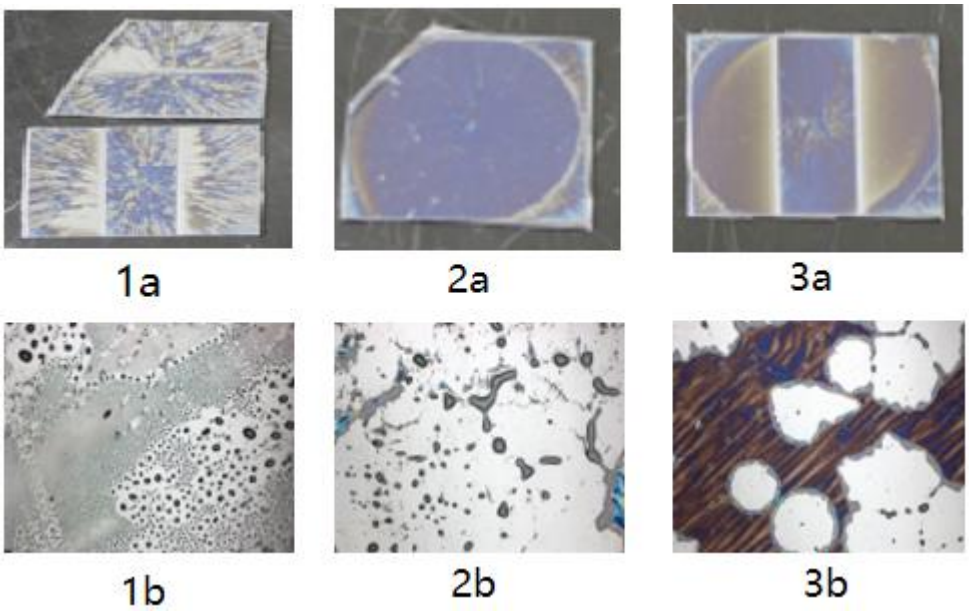

Figure 4.8 ND embedded EVA film adhesion on silicon substrate

From Figure 4.8, samples 2 and 3 have a better coverage than sample 1. Two pieces of sample 1 have been prepared just for crossing out the possibility that poor substrate cleanliness causes the bad coverage. After being cured, sample 3 have the most solid content on the glass substrate while that of sample 1 has the least.

The adhesion of the cured EVA films was performed using tape tests. As showed in the Figure 4.9 (1a), (2a), (3a) are the optical microscopy images of samples 1, 2, and 3, respectively. Figures 4.9 (1b), (2b), and (3b) are the EVA films after being taped peeled 20 times.

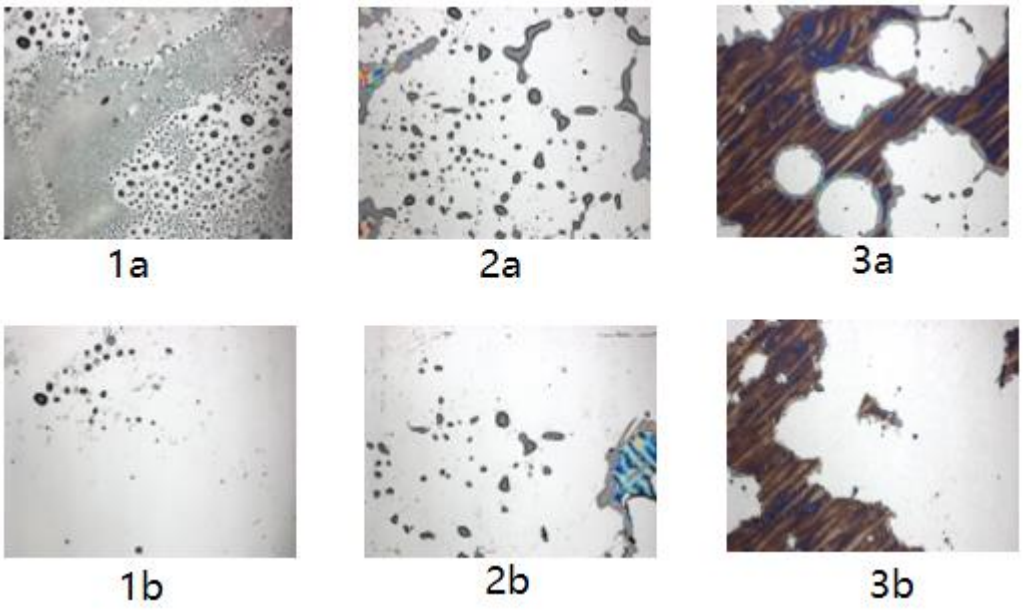

Figure 4.9 ND embedded EVA films after tape peeling tests

From sample 1 to sample 3, EVA sheet changes from small dots into big blocks. Note that these figures are taken using the same optical magnification. Compared with small EVA dots, big EVA blocks are more difficult to be removed by the tape. Sample 3 has the biggest block EVA sheet as it has the most weight percentage of nano diamond particles.

4.4.5 Degradation Study of Nano Diamond Embedded EVA Encapsulation.

Four samples of glass-EVA-glass stacks are prepared. Sample 1 and sample 2 use primitive EVA sheets, and samples 3 and 4 use nano diamond embedded EVA sheets. Samples are exposed in room environment for four years (from May 2013 to May 2017). The light transmittance of the four samples is measured as shown in Figure 4.10. As shown by these plots, all transmittance of the four samples is decreased compared with the transmittance (90%) of the new EVA encapsulation. The difference between degraded primitive EVA and degraded ND embedded EVA occurs between the wavelength from 350nm to 500nm. The

ND embedded EVA shows 20% to 30% better light transmittance than EVA.

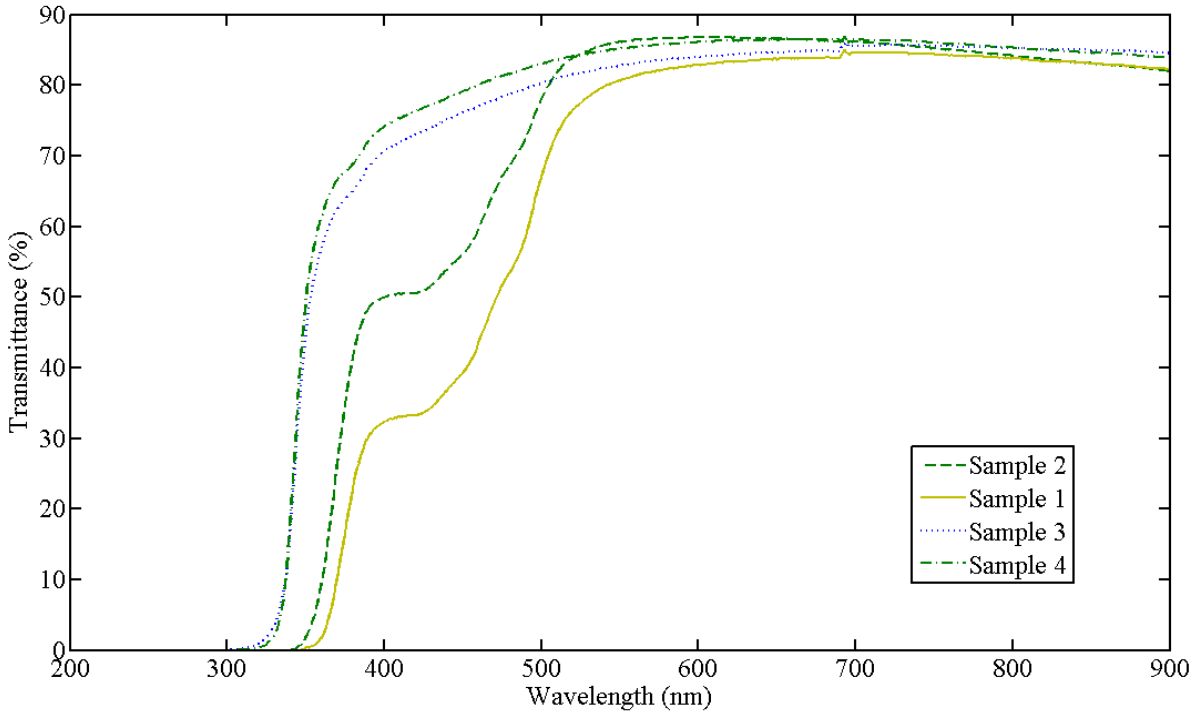

Figure 4.10 Light transmittance of degraded EVA encapsulations

Adhesion strength between EVA and glass is measured using a pull test. After four year of room-temperature degradation, the adhesion strength between ND embedded EVA sheet and glass is average above 1.0×10^6 N/m^2, while the adhesion between primitive EVA and glass has been decreased to 2.3×10^5 N/m^2.

The light transmittance and adhesion strength measurement shows that the embedded ND particles enhance the performance of the EVA encapsulation.

4.5 Nano Silica Embedded EVA Encapsulation

4.5.1 Preparation of Nano Silica Embedded EVA Encapsulation

There are two major steps to prepare the nano silica embedded EVA encapsulation. First,

nano silica particles are first embedded into the EVA sheets. Then, the EVA sheet is laminated between the tempered glass and solar cells.

Preparing a silica/EVA nanocomposite. First, a 5% weight EVA is dissolved in dichloromethane and mixed in an acoustic mixer for about 60 minutes. After that, 0.01% weight nano silica particle is added, and the solution is ultra-sonicated for 15 minutes. The solution is poured out onto a glass panel and the solvent was dried out in an oven. Thirty minutes later, a nano silica embedded EVA film is formed.

The characteristics of the nanosilica/ EVA film were evaluated in a sandwiched structure between the solar cell and the tempered glass as in a photovoltaic (PV) panel. Several laminated structures were made from the nano silica embedded EVA and pristine EVA. To form the laminated structures, the stacks were placed in a vacuum oven, with weights applied to the top of the laminated structures. The lamination process first consisted of a pump-down to below 3 mmHg. This was followed by a quick ramp up to 120°C and held for 20 minutes to melt the EVA sheet as well as to remove potential air bubbles. After that, the temperature was increased to 150°C, and held for 1 hour until the copolymer was well cross linked. Then, the laminated structures were allowed to cool down. Finally, the vacuum was released.

4.5.2 Test Results and Discussion

a) Light Transmittance

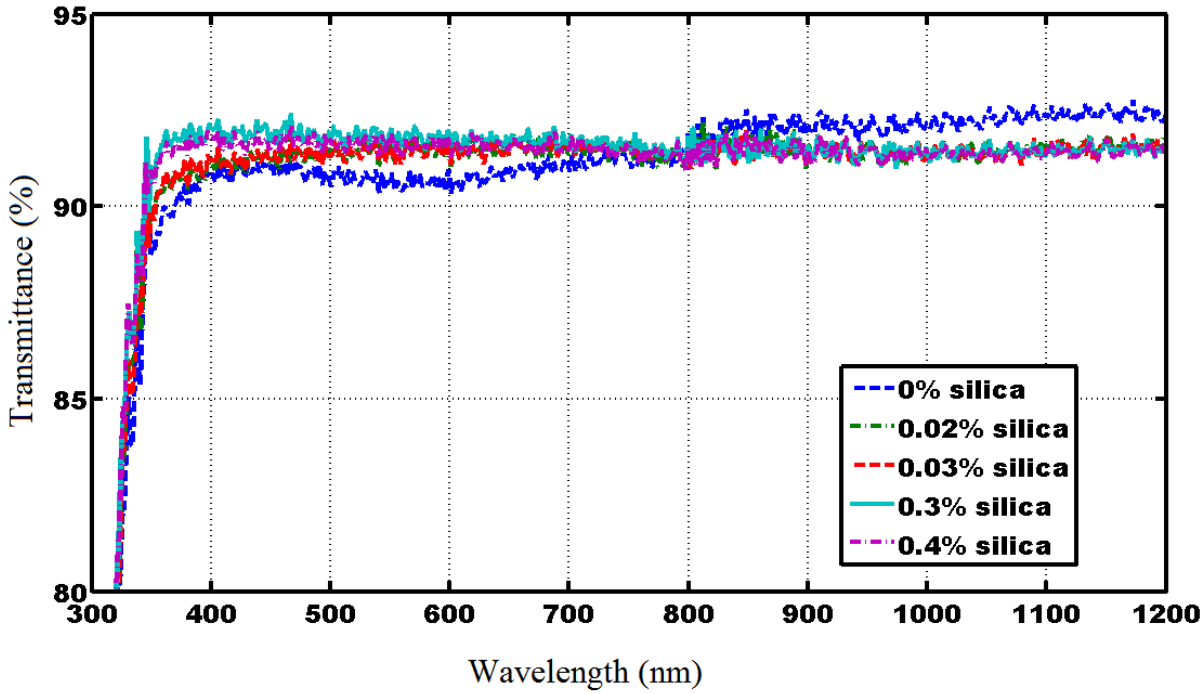

Figure 4.11 Transmittance of EVA films with nano silica fillings. [3.1]

Figure 4.111 shows the transmittance of various glass/EVA laminated samples with nano silica embedded EVA and pristine EVA. As can be seen, the nano silica embedded EVA shows a slight (approximately 1.5%) increase in optical transmittance.

b) Adhesion Between Silica Embedded EVA Film and Glass Substrates.

Pull tests indicates that after embedding silica nanoparticles into the EVA sheet, the adhesion strength remains the same.

4.5.3 Degradation Study of Silica Nano Particles Embedded EVA Encapsulation

After 1000 hours of UVA radiation at the intensity of 2.7Mw/cm^2, the silica embedded EVA encapsulation shows 1% high light transmittance than the pristine EVA encapsulation. Considering the quantity of the radiation approximately equals to 6 months, this UVA test

will continue to yield more convincing data.

4.6 References

[4.1] Wikipedia, Ethylene-vinyl_acetate, https://en.wikipedia.org/wiki /Ethylene-vinyl _acetate.

[4.2] Plastics historical society, http://plastiquarian.com/?page_id=14280

[4.3] F. J. Pern, "Ethylene-vinyl acetate (EVA) encapsulants for photovoltaic modules: Degradation and discoloration mechanisms and formulation modifications for improved photostability," Die Angewandte Makromolekulare Chemie, vol. 252, no. 1, pp. 195–216, Dec. 1997.

[4.4] H. J. Wenger, J. Schaefer, A. Rosenthal, B. Hammond, and L. Schlueter, "Decline of the Carrisa Plains PV power plant: the impact of concentrating sunlight on flat plates," in Conference Record of the 22nd IEEE Photovoltaic Specialists Conference, Las Vegas, NV, 1991, pp. 586–592.

[4.5] J. Pern, "Module Encapsulation Materials, Processing and Testing," Shanghai, China, 2008.

[4.6] D. L. King, M. A. Quintana, J. A. Kratochvil, D. E. Ellibee, and B. R. Hansen, "Photovoltaic module performance and durability following long-term field exposure," National center for photovoltaics (NCPV) 15th program review meeting, Denver, CO, 1999, pp. 565–571.

[4.7] Pern, F. J. (1997), Ethylene-vinyl acetate (EVA) encapsulants for photovoltaic modules: Degradation and discoloration mechanisms and formulation modifications for improved photostability. Angew. Makromol. Chem., 252: 195–216. doi:10.1002/apmc.1997.052520114.

[4.8] A.W. Czanderna, F.J. Pern, "Encapsulation of PV modules using ethylene vinyl acetate copolymer as a pottant: A critical review", Solar Energy Materials and Solar Cells, 43 (1996). 101-183. (NRELJTP-412-7359)

[4.9] GCH 6101-Polymer DiffusionPM Wood-Adams2.

[4.10] Yanbin Cui, S.I. Kundalwal, S. Kumara, "Gas Barrier Performance of Graphene/Polymer Nanocomposites", Carbon, Volume 98, March 2016, Pages 313–333.

[4.11] Mochalin VN, Neitzel I, Etzold BJ, Peterson A, Palmese G, Gogotsi Y. "Covalent incorporation of aminated nanodiamond into an epoxy polymer network", ACS Nano. 2011

Sep 27;5(9):7494-502. doi: 10.1021/nn2024539. Epub 2011 Aug 16.

[4.12] Maitra U., Prasad K. E., Ramamurty U., Rao C. N. R. “Mechanical Properties of Nanodiamond-Reinforced Polymer-Matrix Composites”. Solid State Commun. 2009, 149, 1693–1697.

[4.13] Spitalsky Z., Kromka A., Matejka L., Cernoch P., Kovarova J., Kotek J., Slouf M. “Effect of Nanodiamond Particles on Properties of Epoxy Composites”. Adv. Compos. Lett. 2008, 17, 29–34.

[4.14] Vadym N. Mochalin, Olga Shenderova, Dean Ho, Yury Gogotsi, “The properties and applications of nanodiamonds”. Nature Nanotechnology 7, 11–23 (2012) doi:10.1038/nnano.2011.209 Published online 18 December 2011

[4.15] Osswald, S., Yushin, G., Mochalin, V., Kucheyev, S. O., Gogotsi, Y. “Control of sp2/sp3 Carbon Ratio and Surface Chemistry of Nanodiamond Powders by Selective Oxidation in Air”. J. Am. Chem. Soc. 2006, 128, 11635–11642.

Chapter 5. Conclusions and Recommendations for Future Work

The aim of the dissertation work is to develop innovative nanomaterials for packaging the photovoltaic (PV) panels to improve its overall performance. Two types of photovoltaic panel packaging materials are developed and investigated to realize this objective. The first is the hydrophobic/anti-reflective surface coating which not only repels water from the top glass of a PV panel but at the same time reduces the light reflectance between the top glass and air ambient. The second packaging material is the nano particle embedded EVA encapsulation material with preferable mechanical and degradation properties.

5.1 Hydrophobic/Anti-Reflective Coating

COMSOL simulation tool is used to understand the relations between configuration of ellipsoid-shaped nano structures and light reflectance, and how a polymer layer on top of the nano structures affects the optical property of the coating. The results indicate that taller ellipsoid rod (aspect ratio = 5) reflects less light than shorter rod (aspect ratio = 0.5) in the desired spectrum for solar energy harvest (400nm-700nm wavelength). The polymer layer increases the light transmittance when the light incident angle is from 23° to 34°. As such, with a polymer layer, light is able to propagate though the glass with a high transmittance at an incident angle from 0° to 34° compared to the scenario without the polymer layer when the light transmittance decreases if the incident angle is larger than 23°. In practical application, this polymer layer will largely increase the PV module efficiency in the early morning or late afternoon when the incident angles are large. This is the first time to our

knowledge that COMSOL simulation is used to simulate a combined nanostructure and polymer anti-reflective structure. For future work, a parabolic-shaped nano structure deserves further investigation due to its unique shape advantage in optical component design. Also, patterned polymer material may improve the light transmittance.

There are many reports focused either only on the design of a hydrophobic surface or an anti-reflective surface. In this research work, the design of a combined anti-reflective and hydrophobic surface for PV panel is investigated. This approach may inspire future surface coating design to consider both the surface wetting and optical properties for application-specific purposes. For example, the surface coating can be focus more on its wetting property than its optical property for dusty or icy applications or be more optical property orientated in dry and clean air environments.

A sol-gel process is developed to prepare a hydrophobic/anti-reflective coating. The light transmittance of the coated glass slides is 3% higher (between the wavelength 400nm-700nm) than that for a bare glass slide. This is the same improvement in transmittance (if not better than) than similar surface coatings on the market. For example, the 94.9% overall light transmittance of our coating is higher than Pilkinton's Sunplus glass with a light transmittance of 93.9%. The water contact angle of the sol-gel prepared coating reaches 150° which indicates that it is a super hydrophobic coating. The coating passed the MIL-STD-810G felt abrasion test, 100 cycles of temperature cycling test (-45°C-120°C), heat test (200°C for 500 hours), and UV test (2.7Mw/cm2 UVA radiation for 1000 hours). Furthermore, all the variations (silica thickness, polystyrene concentration, SAM growing

time) are investigated as factors that affect transmittance and water contact angle. The established methodology in this research can be used in future coating research.

A nanoimprinting process is developed and used for preparing a silicone material based hydrophobic/anti-reflective coating. The resultant coating increases the light transmittance of bare glass slides by 1.5% with a water contact angle above 150°. This nanoimprinting method has the potential of large scale production in industry. However, the silicone material is relatively soft, cannot resist the environment weathering very well. In future, a better moldable material instead of silicone or nanocomposite materials can be used to enhance the mechanic property of silicone. In this process, DRIE etching and wet etching are used together to create a new and unique silicon surface configuration. This surface is used as a mold for this research work, but due to its super low light reflectance, it can also be used as anti-reflective pattern on the silicon solar cell, or other plasmonic structure research.

5.2 Nanoparticle embedded EVA encapsulation

Silica nano particles and functionalized nano diamonds are embedded respectively into the EVA matrix to reduce the degradation rate of the polymer. This is a new approach to protect the EVA from aging, compare with traditional methods which use additives to react with free radicals that may harm the EVA. The embedded particles block the path of radicals and prevent them from moving through the matrix and creating damage. UV tests for 2 months at 2.7 mW/cm^2 indicate that the EVA with silica or nano diamond particles doping degrades

slightly slower than the primitive EVA sheet. The difference is a 1% light transmittance difference after UV radiation between the nano-particle embedded EVA and the pristine EVA encapsulation. UV test should be continued further to yield more convincing data. The embedded EVA sheet exhibits better adhesion strength with glass surface indicated by a conventional tape peeling test. In the future, graphene or graphene oxide nano flakes with different surface functionalization can be studied as fillings in the EVA nanocomposite. The optical, chemical, and mechanical properties of these nano materials may serve as a good radical blocker.

Chapter 6. Appendix

COMSOL Simulation Report

Reflectance simulation of a silica coated glass slide.

(a) Global Definitions

Date	Mar 13, 2017 3:23:05 PM

Global settings

Name	Sample 1.mph
Path	G:\March\Sample 1\sample 1.mph
COMSOL version	COMSOL 5.2a (Build: 199)

Used products

COMSOL Multiphysics
Wave Optics Module

Parameters

Name	Expression	Value	Description
Na	1	1	Refractive index, air
Nb	1.2	1.2	Refractive index,dielectric
D	0.11[um]	1.1E−7 m	Grating constant
lam0	100[nm]	1E−7 m	Vacuum wavelength
f0	c_const/lam0	2.9979E15 1/s	Frequency
Alpha	0	0	Angle of incidence
Beta	asin(na*sin(alpha)/nb)	0 rad	Refraction angle

（b）Component

Component settings

Unit system	SI

Definitions

Selections

Explicit 1

Selection type
Explicit

Selection
Boundaries 22–24

Explicit 2

Selection type
Explicit

Selection
Boundaries 15–17

Coordinate Systems

Boundary System 1

Coordinate system type	Boundary system
Tag	sys1

Coordinate names

First	Second	Third
t1	t2	N

Geometry 1

Units

Length unit	M
Angular unit	Deg

Geometry statistics

Description	Value
Space dimension	3
Number of domains	4
Number of boundaries	24
Number of edges	40
Number of vertices	21

Block 3 (blk3)

Position

Description	Value
Position	{0, 0, -750*d}
Base	Center

Axis

Description	Value
Axis type	z – axis

Size and shape

Description	Value
Width	3*d
Depth	3*d
Height	1500*d

Block 4 (blk4)

Position

Description	Value
Position	{0, 0, 20*d}
Base	Center

Axis

Description	Value
Axis type	z – axis

Size and shape

Description	Value
Width	3*d
Depth	3*d
Height	40*d

Sphere 1 (sph1)

Position

Description	Value
Position	{0, 0, 0}

Axis

Description	Value
Axis type	z – axis

Size

Description	Value
Radius	1.5*d

Block 5 (blk5)

Position

Description	Value
Position	{0, 0, -150*d}
Base	Center

Axis

Description	Value
Axis type	z – axis

Size and shape

Description	Value

Width	3*d
Depth	3*d
Height	300*d

Block 6 (blk6)

Position

Description	Value
Position	{0, 0, 10*d}
Base	Center

Axis

Description	Value
Axis type	z – axis

Size and shape

Description	Value
Width	3*d
Depth	3*d
Height	20*d

Materials

air (Ciddor)

Selection

Geometric entity level	Domain
Selection	Domains 2–3

Material parameters

Name	Value	Unit
Refractive index, real part	1	1
Refractive index, imaginary part	k_interp(1[1/m]*c_const/freq)	1

Refractive index Settings

Description	Value
Refractive index, real part	{{1, 0, 0}, {0, 1, 0}, {0, 0, 1}}
Refractive index, imaginary part	{{k_interp(1[1/m]*c_const/freq), 0, 0}, {0, k_interp(1[1/m]*c_const/freq), 0}, {0, 0, k_interp(1[1/m]*c_const/freq)}}

soda-lime (Rubin-clear)

Selection

Geometric entity level	Domain
Selection	Domains 1, 4

Material parameters

Name	Value	Unit
Refractive index, real part	n_interp(1[1/m]*c_const/f	1

	req)	
Refractive index, imaginary part	k_interp(1[1/m]*c_const/freq)	1

Refractive index Settings

Description	Value
Refractive index, real part	{{n_interp(1[1/m]*c_const/freq), 0, 0}, {0, n_interp(1[1/m]*c_const/freq), 0}, {0, 0, n_interp(1[1/m]*c_const/freq)}}
Refractive index, imaginary part	{{k_interp(1[1/m]*c_const/freq), 0, 0}, {0, k_interp(1[1/m]*c_const/freq), 0}, {0, 0, k_interp(1[1/m]*c_const/freq)}}

Electromagnetic Waves, Frequency Domain

Used products

COMSOL Multiphysics
Wave Optics Module

Electromagnetic Waves, Frequency Domain

Selection

Geometric entity level	Domain
Selection	Domains 1–4

Equations

$$\nabla \times \mu_r^{-1}(\nabla \times \mathbf{E}) - k_0^2(\epsilon_r - \frac{j\sigma}{\omega\epsilon_0})\mathbf{E} = \mathbf{0}$$

Settings

Description	Value
Electric field	Quadratic
Value type when using splitting of complex variables	Complex
Solve for	Full field
Activate port sweep	Off
Enable	Off

Wave Equation, Electric 1

Selection

Geometric entity level	Domain
Selection	Domains 1–4

Equations

$$\nabla \times (\nabla \times \mathbf{E}) - k_0^2 \varepsilon_r \mathbf{E} = \mathbf{0}$$

Settings

Description	Value
Electric displacement field model	Refractive index
Refractive index, real part	From material
Refractive index, imaginary part	From material

Properties from material

Property	Material	Property group
Refractive index, real part	air (Ciddor)	Refractive index
Refractive index, imaginary part	air (Ciddor)	Refractive index
Refractive index, real part	soda-lime (Rubin-clear)	Refractive index
Refractive index, imaginary part	soda-lime (Rubin-clear)	Refractive index

Variables

Shape functions

Name	Shape function	Unit	Description	Shape frame	Selection
Ex	Curl (Quadratic)	V/m	Electric field, x component	Material	Domains 1–4
Ey	Curl (Quadratic)	V/m	Electric field, y component	Material	Domains 1–4
Ez	Curl (Quadratic)	V/m	Electric field, z component	Material	Domains 1–4

Weak expressions

Weak expression	Integration order	Integration frame	Selection
-mu0_const*(-ewfd.dHdtx*ewfd.curltestdepEx-ewfd.dHdty*ewfd.curltestdepEy-ewfd.dHdtz*ewfd.curltestdepEz+ewfd.iomega*(ewfd.Jx*ewfd.testdepEx+ewfd.Jy*ewfd.testdepEy+ewfd.Jz*ewfd.testdepEz))	4	Material	Domains 1–4

Perfect Electric Conductor 1

Selection

Geometric entity level	Boundary
Selection	No boundaries

Equations

$$\mathbf{n} \times \mathbf{E} = \mathbf{0}$$

Settings

Description	Value
Apply reaction terms on	All physics (symmetric)
Use weak constraints	Off
Constraint method	Elemental

Initial Values 1

Selection

Geometric entity level	Domain
Selection	Domains 1–4

Port 1

Selection

Geometric entity level	Boundary
Selection	Boundary 10

Equations

$$S = \frac{\int_{\partial\Omega} (\mathbf{E} - \mathbf{E}_1) \cdot \mathbf{E}_1}{\int_{\partial\Omega} \mathbf{E}_1 \cdot \mathbf{E}_1}$$

Settings

Description	Value
Port name	1
Wave excitation at this port	On
Port input power	100[W]
Mode phase	0
Specify deposited power	Off
Activate slit condition on interior port	Off
Type of port	Periodic
Input quantity	Electric field
Electric mode field amplitude	{sin(pi/4), cos(pi/4), 0}
Elevation angle of incidence	alpha

Azimuth angle of incidence	0
Refractive index, real part	{{1, 0, 0}, {0, 1, 0}, {0, 0, 1}}
Maximum frequency	f0

Variables

Weak expressions

Weak expression	Integration order	Integration frame	Selection
ewfd.iomega*mu0_const*(-(ewfd.tHmodez_1*ewfd.ny-ewfd.tHmodey_1*ewfd.nz)*conj(ewfd.tEmodex_1)-(-ewfd.tHmodez_1*ewfd.nx+ewfd.tHmodex_1*ewfd.nz)*conj(ewfd.tEmodey_1)-(ewfd.tHmodey_1*ewfd.nx-ewfd.tHmodex_1*ewfd.ny)*conj(ewfd.tEmodez_1))*test(1+if(abs(arg(ewfd.beta_1))<=0.25*pi||abs(arg(ewfd.beta_1))>=0.75*pi,ewfd.S1x,0))*(-1+if(abs(arg(ewfd.beta_1))<=0.25*pi||abs(arg(ewfd.beta_1))>=0.75*pi,ewfd.S1x,0))	4	Material	Boundary 10

Shape functions

Constraint	Constraint force	Shape function	Selection
tEx-ewfd.PortConstrx	test(tEx)-ewfd.PortConstrx_weak	Curl (Quadratic)	Boundary 10
tEy-ewfd.PortConstry	test(tEy)-ewfd.PortConstry_weak	Curl (Quadratic)	Boundary 10
tEz-ewfd.PortConstrz	test(tEz)-ewfd.PortConstrz_weak	Curl (Quadratic)	Boundary 10

Port 2

Selection

Geometric entity level	Boundary
Selection	Boundary 3

Equations

$$S = \frac{\int_{\partial\Omega} \mathbf{E} \cdot \mathbf{E}_2}{\int_{\partial\Omega} \mathbf{E}_2 \cdot \mathbf{E}_2}$$

Settings

Description	Value
Port name	2
Wave excitation at this port	Off
Mode phase	0
Activate slit condition on interior port	Off
Type of port	Periodic
Input quantity	Electric field
Electric mode field amplitude	{cos(pi/4), sin(pi/4), 0}
Elevation angle of incidence	-beta
Azimuth angle of incidence	0
Refractive index, real part	{{n_interp(1[1/m]*c_const/freq), 0, 0}, {0, n_interp(1[1/m]*c_const/freq), 0}, {0, 0, n_interp(1[1/m]*c_const/freq)}}
Maximum frequency	f0

Variables

Weak expressions

Weak expression	Integration order	Integration frame	Selection
ewfd.iomega*mu0_const*(-(ewfd.tHmodez_2*ewfd.ny-ewfd.tHmodey_2*ewfd.nz)*conj(ewfd.tEmodex_2)-(-ewfd.tHmodez_2*ewfd.nx+ewfd.tHmodex_2*ewfd.nz)*conj(ewfd.tEmodey_2)-(ewfd.tHmodey_2*ewfd.nx-ewfd.tHmodex_2*ewfd.ny)*conj(ewfd.tEmodez_2))*test(if(abs(arg(ewfd.beta_2))<=0.25*pi||abs(arg(ewfd.beta_2))>=0.75*pi,ewfd.S2x,0))*if(abs(arg(ewfd.beta_2))<=0.25*pi||abs(arg(ewfd.beta_2))>=0.75*pi,ewfd.S2x,0)	4	Material	Boundary 3

Shape functions

Constraint	Constraint force	Shape function	Selection
tEx-ewfd.PortConstrx	test(tEx)-ewfd.PortConstrx_weak	Curl (Quadratic)	Boundary 3

tEy-ewfd.PortConstry	test(tEy)-ewfd.PortConstry_weak	Curl (Quadratic)	Boundary 3
tEz-ewfd.PortConstrz	test(tEz)-ewfd.PortConstrz_weak	Curl (Quadratic)	Boundary 3

Periodic Condition 1

Selection

Geometric entity level	Boundary
Selection	Boundaries 1, 4, 7, 22–24

Equations

$$\mathbf{E}_{dst} = \mathbf{E}_{src} e^{-i\mathbf{k}_F \cdot (\mathbf{r}_{dst} - \mathbf{r}_{src})}$$

$$\mathbf{H}_{dst} = \mathbf{H}_{src} e^{-i\mathbf{k}_F \cdot (\mathbf{r}_{dst} - \mathbf{r}_{src})}$$

Settings

Description	Value
Type of periodicity	Floquet periodicity
k-vector for Floquet periodicity	From periodic port
Apply reaction terms on	All physics (symmetric)
Constraint method	Nodal
Transform to intermediate map	Automatic

Variables

Name	Expression	Unit	Description	Selection
ewfd.kFloquetx	ewfd.kPeriodicx	rad/m	k-vector for Floquet periodicity, x component	Boundaries 1, 4, 7
ewfd.kFloquety	ewfd.kPeriodicy	rad/m	k-vector for Floquet periodicity, y component	Boundaries 1, 4, 7
ewfd.kFloquetz	ewfd.kPeriodicz	rad/m	k-vector for Floquet periodicity, z component	Boundaries 1, 4, 7
ewfd.kFloquetx	ewfd.kPeriodicx	rad/m	k-vector for Floquet periodicity, x component	Boundaries 22–24
ewfd.kFloquety	ewfd.kPeriodicy	rad/m	k-vector for Floquet periodicity, y component	Boundaries 22–24
ewfd.kFloquetz	ewfd.kPeriodicz	rad/m	k-vector for Floquet periodicity, z component	Boundaries 22–24

Shape functions

Constraint	Constraint force	Shape function	Selection
if(root.comp1.ewfd.incontact_pc1,ewfd.tEsdimx-ewfd.dst2src_pc1(ewfd.tEsdimx)*exp(j*(-ewfd.kFloquetx*(ewfd.rsrcx_pc1-ewfd.rdstx_pc1)-ewfd.kFloquety*(ewfd.rsrcy_pc1-ewfd.rdsty_pc1)-ewfd.kFloquetz*(ewfd.rsrcz_pc1-ewfd.rdstz_pc1))),0)	if(root.comp1.ewfd.incontact_pc1,test(ewfd.tEsdimx)*exp(j*(-ewfd.kFloquetx*(ewfd.rsrcx_pc1-ewfd.rdstx_pc1)-ewfd.kFloquety*(ewfd.rsrcy_pc1-ewfd.rdsty_pc1)-ewfd.kFloquetz*(ewfd.rsrcz_pc1-ewfd.rdstz_pc1)))-test(ewfd.dst2src_pc1(ewfd.tEsdimx)),0)	Curl (Quadratic)	Boundaries 1, 4, 7
if(root.comp1.ewfd.incontact_pc1,ewfd.tEsdimy-ewfd.dst2src_pc1(ewfd.tEsdimy)*exp(j*(-ewfd.kFloquetx*(ewfd.rsrcx_pc1-ewfd.rdstx_pc1)-ewfd.kFloquety*(ewfd.rsrcy_pc1-ewfd.rdsty_pc1)-ewfd.kFloquetz*(ewfd.rsrcz_pc1-ewfd.rdstz_pc1))),0)	if(root.comp1.ewfd.incontact_pc1,test(ewfd.tEsdimy)*exp(j*(-ewfd.kFloquetx*(ewfd.rsrcx_pc1-ewfd.rdstx_pc1)-ewfd.kFloquety*(ewfd.rsrcy_pc1-ewfd.rdsty_pc1)-ewfd.kFloquetz*(ewfd.rsrcz_pc1-ewfd.rdstz_pc1)))-test(ewfd.dst2src_pc1(ewfd.tEsdimy)),0)	Curl (Quadratic)	Boundaries 1, 4, 7
if(root.comp1.ewfd.incontact_pc1,ewfd.tEsdimz-ewfd.dst2src_pc1(ewfd.tEsdimz)*exp(j*(-ewfd.kFloquetx*(ewfd.rsrcx_pc1-ewfd.rdstx_pc1)-ewfd.kFloquety*(ewfd.rsrcy_pc1-ewfd.rdsty_pc1)-ewfd.kFloquetz*(ewfd.rsrcz_pc1-ewfd.rdstz_pc1))),0)	if(root.comp1.ewfd.incontact_pc1,test(ewfd.tEsdimz)*exp(j*(-ewfd.kFloquetx*(ewfd.rsrcx_pc1-ewfd.rdstx_pc1)-ewfd.kFloquety*(ewfd.rsrcy_pc1-ewfd.rdsty_pc1)-ewfd.kFloquetz*(ewfd.rsrcz_pc1-ewfd.rdstz_pc1)))-test(ewfd.dst2src_pc1(ewfd.tEsdimz)),0)	Curl (Quadratic)	Boundaries 1, 4, 7

Periodic Condition 2

Selection

Geometric entity level	Boundary

Selection	Boundaries 2, 5, 8, 15–17

Equations

$$\mathbf{E}_{dst} = \mathbf{E}_{src} e^{-j\mathbf{k}_F \cdot (\mathbf{r}_{dst} - \mathbf{r}_{src})}$$

$$\mathbf{H}_{dst} = \mathbf{H}_{src} e^{-j\mathbf{k}_F \cdot (\mathbf{r}_{dst} - \mathbf{r}_{src})}$$

Settings

Description	Value
Type of periodicity	Floquet periodicity
k-vector for Floquet periodicity	From periodic port
Apply reaction terms on	All physics (symmetric)
Constraint method	Nodal
Transform to intermediate map	Automatic

Variables

Name	Expression	Unit	Description	Selection
ewfd.kFloquetx	ewfd.kPeriodicx	rad/m	k-vector for Floquet periodicity, x component	Boundaries 2, 5, 8
ewfd.kFloquety	ewfd.kPeriodicy	rad/m	k-vector for Floquet periodicity, y component	Boundaries 2, 5, 8
ewfd.kFloquetz	ewfd.kPeriodicz	rad/m	k-vector for Floquet periodicity, z component	Boundaries 2, 5, 8
ewfd.kFloquetx	ewfd.kPeriodicx	rad/m	k-vector for Floquet periodicity, x component	Boundaries 15–17
ewfd.kFloquety	ewfd.kPeriodicy	rad/m	k-vector for Floquet periodicity, y component	Boundaries 15–17
ewfd.kFloquetz	ewfd.kPeriodicz	rad/m	k-vector for Floquet periodicity, z component	Boundaries 15–17

Shape functions

Constraint	Constraint force	Shape function	Selection
if(root.comp1.ewfd.incontact_pc2,ewfd.tEsdimx-ewfd.dst2src_pc2(ewfd.tEsdimx)*exp(j*(-ewfd.kFloquetx*(ewfd.rsrcx_pc2-ewf	if(root.comp1.ewfd.incontact_pc2,test(ewfd.tEsdimx)*exp(j*(-ewfd.kFloquetx*(ewfd.rsrcx_pc2-ewfd.rdstx_pc2)-ewfd.kFloquet	Curl (Quadratic)	Boundaries 2, 5, 8

d.rdstx_pc2)-ewfd.kFloquety*(ewfd.rsrcy_pc2-ewfd.rdsty_pc2)-ewfd.kFloquetz*(ewfd.rsrcz_pc2-ewfd.rdstz_pc2))),0)	y*(ewfd.rsrcy_pc2-ewfd.rdsty_pc2)-ewfd.kFloquetz*(ewfd.rsrcz_pc2-ewfd.rdstz_pc2)))-test(ewfd.dst2src_pc2(ewfd.tEsdimx)),0)		
if(root.comp1.ewfd.incontact_pc2,ewfd.tEsdimy-ewfd.dst2src_pc2(ewfd.tEsdimy)*exp(j*(-ewfd.kFloquetx*(ewfd.rsrcx_pc2-ewfd.rdstx_pc2)-ewfd.kFloquety*(ewfd.rsrcy_pc2-ewfd.rdsty_pc2)-ewfd.kFloquetz*(ewfd.rsrcz_pc2-ewfd.rdstz_pc2))),0)	if(root.comp1.ewfd.incontact_pc2,test(ewfd.tEsdimy)*exp(j*(-ewfd.kFloquetx*(ewfd.rsrcx_pc2-ewfd.rdstx_pc2)-ewfd.kFloquety*(ewfd.rsrcy_pc2-ewfd.rdsty_pc2)-ewfd.kFloquetz*(ewfd.rsrcz_pc2-ewfd.rdstz_pc2)))-test(ewfd.dst2src_pc2(ewfd.tEsdimy)),0)	Curl (Quadratic)	Boundaries 2, 5, 8
if(root.comp1.ewfd.incontact_pc2,ewfd.tEsdimz-ewfd.dst2src_pc2(ewfd.tEsdimz)*exp(j*(-ewfd.kFloquetx*(ewfd.rsrcx_pc2-ewfd.rdstx_pc2)-ewfd.kFloquety*(ewfd.rsrcy_pc2-ewfd.rdsty_pc2)-ewfd.kFloquetz*(ewfd.rsrcz_pc2-ewfd.rdstz_pc2))),0)	if(root.comp1.ewfd.incontact_pc2,test(ewfd.tEsdimz)*exp(j*(-ewfd.kFloquetx*(ewfd.rsrcx_pc2-ewfd.rdstx_pc2)-ewfd.kFloquety*(ewfd.rsrcy_pc2-ewfd.rdsty_pc2)-ewfd.kFloquetz*(ewfd.rsrcz_pc2-ewfd.rdstz_pc2)))-test(ewfd.dst2src_pc2(ewfd.tEsdimz)),0)	Curl (Quadratic)	Boundaries 2, 5, 8

Mesh

Size (size)

Settings

Description	Value
Maximum element size	441[nm]/5
Minimum element size	441[nm]/10
Curvature factor	0.4
Resolution of narrow regions	0.7
Maximum element growth rate	1.4
Predefined size	Finer
Custom element size	Custom

Free Triangular 1 (ftri1)

Selection

Geometric entity level	Boundary
Selection	Boundaries 1, 4, 7

Free Triangular 1

Free Triangular 2 (ftri2)

Selection

Geometric entity level	Boundary
Selection	Boundaries 2, 5, 8

Free Triangular 2

Free Tetrahedral 1 (ftet1)

Selection

Geometric entity level	Remaining

Free Tetrahedral 1

Settings

Description	Value
Method	Delaunay (legacy version)

(c) Study

Study 1

Computation information

Computation time	44 min 2 s
CPU	Intel(R) Core(TM) i7-4790S CPU @ 3.20GHz, 4 cores
Operating system	Windows 7

Parametric Sweep

Parameter name	Parameter value list
alpha	range(0,0.19634954084936207,0.7853981633974483)

Wavelength Domain

Study settings

Description	Value
Include geometric nonlinearity	Off

Wavelengths: lam0 lam0*2 lam0*3 lam0*4 lam0*5 lam0*6 lam0*7 lam0*8 lam0*9 lam0*10 lam0*11 lam0*12

Physics and variables selection

Physics interface	Discretization
Electromagnetic Waves, Frequency Domain (ewfd)	physics

Mesh selection

Geometry	Mesh
Geometry 1 (geom1)	mesh1

Solver Configurations

Solution 1

Compile Equations: Wavelength Domain (st1)

Study and step

Description	Value
Use study	
Use study step	

Dependent Variables 1 (v1)

General

Description	Value
Defined by study step	

Initial value calculation constants

Description	Value
Parameter initial value list	lam0 lam0*2 lam0*3 lam0*4 lam0*5 lam0*6 lam0*7 lam0*8 lam0*9 lam0*10 lam0*11 lam0*12

Electric field (comp1.E) (comp1_E)

General

Description	Value

Field components	{comp1.Ex, comp1.Ey, comp1.Ez}

S-parameter (comp1.Sparam1) (comp1_Sparam1)

General

Description	Value
State components	comp1.ewfd.S1x

S-parameter (comp1.Sparam2) (comp1_Sparam2)

General

Description	Value
State components	comp1.ewfd.S2x

Stationary Solver 1 (s1)

General

Description	Value
Defined by study step	

Results while solving

Description	Value
Probes	None

Advanced (aDef)

Assembly settings

Description	Value
Allow complex-valued output from functions with real input	On

Parametric 1 (p1)

General

Description	Value
Defined by study step	
Parameter value list	lam0 lam0*2 lam0*3 lam0*4 lam0*5 lam0*6 lam0*7 lam0*8 lam0*9 lam0*10 lam0*11 lam0*12
Run	No parameter

continuation for	

Fully Coupled 1 (fc1)

General

Description	Value
Linear solver	

Parametric Solutions 1

alpha=0 (su1)

General

Description	Value
Solution	alpha=0

alpha=0.19635 (su2)

General

Description	Value
Solution	alpha=0.19635

alpha=0.3927 (su3)

General

Description	Value
Solution	alpha=0.3927

alpha=0.58905 (su4)

General

Description	Value
Solution	alpha=0.58905

alpha=0.7854 (su5)

General

Description	Value
Solution	alpha=0.7854

(d) Results

Data Sets

Study 1/Solution 1

Solution

Description	Value
Solution	
Component	Save Point Geometry 1

Data set: Study 1/Solution 1

Study 1/Parametric Solutions 1

Solution

Description	Value
Solution	
Component	Save Point Geometry 1

Data set: Study 1/Parametric Solutions 1

Derived Values

Global Evaluation 1

Data

Description	Value
Data set	

Expressions

Expression	Unit	Description
abs(ewfd.S11)^2	1	

Output

Evaluated in	

Tables

Table 1

Global Evaluation 1 (abs(ewfd.S11)^2)

Table 1

alpha	lambda0 (µm)	abs(ewfd.S11)^2 (1)
0.0000	0.10000	0.30760

0.0000	0.20000	0.011065
0.0000	0.30000	0.22745
0.0000	0.40000	0.057059
0.0000	0.50000	0.011722
0.0000	0.60000	0.0043945
0.0000	0.70000	0.0061400
0.0000	0.80000	0.0097903
0.0000	0.90000	0.013602
0.0000	1.0000	0.017136
0.0000	1.1000	0.020177
0.0000	1.2000	0.022770
0.19635	0.10000	0.053594
0.19635	0.20000	0.065050
0.19635	0.30000	0.0014149
0.19635	0.40000	0.23970
0.19635	0.50000	0.014659
0.19635	0.60000	0.0066754
0.19635	0.70000	0.0090121
0.19635	0.80000	0.0090188
0.19635	0.90000	0.013150
0.19635	1.0000	0.015525
0.19635	1.1000	0.019403
0.19635	1.2000	0.026863
0.39270	0.10000	0.038540
0.39270	0.20000	0.029231
0.39270	0.30000	0.0089399
0.39270	0.40000	0.14642
0.39270	0.50000	0.14380
0.39270	0.60000	0.0083296
0.39270	0.70000	0.0029566
0.39270	0.80000	0.025711
0.39270	0.90000	0.023138
0.39270	1.0000	0.026528
0.39270	1.1000	0.017842
0.39270	1.2000	0.022813
0.58905	0.10000	0.24589
0.58905	0.20000	0.20141

0.58905	0.30000	0.28074
0.58905	0.40000	0.59701
0.58905	0.50000	0.012214
0.58905	0.60000	0.024837
0.58905	0.70000	0.014544
0.58905	0.80000	0.045079
0.58905	0.90000	0.062500
0.58905	1.0000	0.038661
0.58905	1.1000	0.0076160
0.58905	1.2000	0.081639
0.78540	0.10000	0.35819
0.78540	0.20000	0.088762
0.78540	0.30000	0.16248
0.78540	0.40000	0.021971
0.78540	0.50000	0.10186
0.78540	0.60000	0.029787
0.78540	0.70000	0.027823
0.78540	0.80000	0.034865
0.78540	0.90000	0.090554
0.78540	1.0000	0.11903
0.78540	1.1000	0.035855
0.78540	1.2000	0.11977

Plot Groups

Electric Field (ewfd)

alpha(5)=0.7854 lambda0(12)=1.2 μm Multislice: Electric field norm (V/m)

1D Plot Group 2

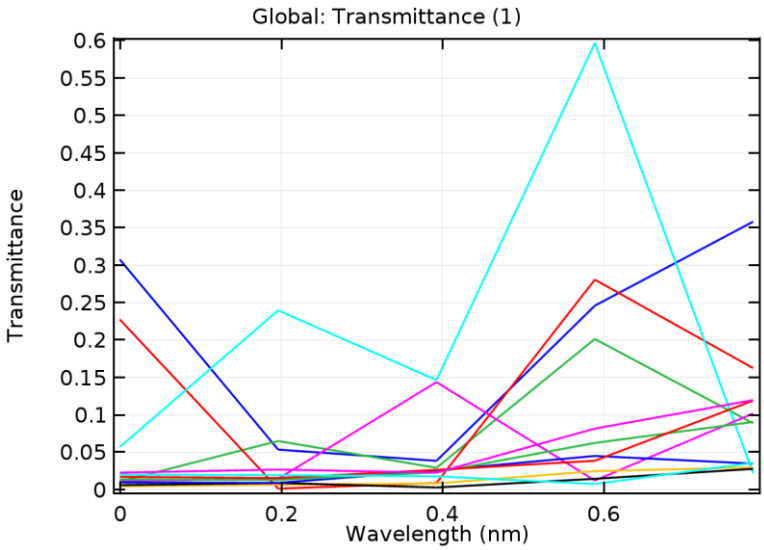

Global: Transmittance (1)

Electric Field (ewfd) 1

lambda0(12)=1.2 µm Multislice: Electric field norm (V/m)

2D Plot Group 4